2012

A Molecular Dynamics Study of Flame Spray Deposition

John Plumeri
Lehigh University

Recommended Citation

Plumeri, John, "A Molecular Dynamics Study of Flame Spray Deposition" (2012). *Theses and Dissertations.* Paper 1088.

A Molecular Dynamics Study of Flame Spray Deposition

by

John Plumeri

A Thesis

Presented to the Graduate and Research Committee

of Lehigh University

In Candidacy for the Degree of

Master of Science

in

Mechanical Engineering and Mechanics

Lehigh University

January 2012

This thesis is accepted and approved in partial fulfillment of the requirement for the Master of Science.

Date

Dr. Edmund B. Webb, III

Thesis Advisor

Dr. Gary Harlow

Department Chair

Acknowledgements

I would like to thank, first and foremost, my family and friends for their love and support, and my advisor Dr. Edmund Webb, III for his continued academic and intellectual guidance. Also, to the faculty and staff of the Mechanical Engineering department at Lafayette College, my eternal thanks for an education which has carried me to where I am today. Finally, unending gratitude to the faculty and staff of the Mechanical Engineering and Mechanics department at Lehigh University for their ongoing education, advice, and help in my ongoing academic career.

Table of Contents

1. Introduction to Thermal Spray Coatings

2. Numerical Simulation Techniques

3. Development of Thermal Spray Model

4. Simulation Results

List of Tables

List of Figures

Abstract

The spreading of molten metallic droplets was studied using molecular dynamics simulation in a cylindrical geometry. The droplets consisted of copper with diameter D = 40 nm at T = 1500 K, modeled using the embedded atom method, spreading on a flat atomic planar surface of aluminum. The surface was maintained as an NVE ensemble and controlled by conduction from a region under Nosé-Hoover thermostat control. The development of the simulation ensemble and the dynamics of an individual reactive drop were analyzed. The substrate was tested for behavior simulating a semi-infinite slab; it was determined that the substrate sufficiently damped internal pressure waves. The test results, as well as the time evolution of drop radius, contact angle, temperature, density, and dissolution with the surface are compared.

1. Introduction to Thermal Spray Coatings

1.1 Introduction to fluid mechanics

Fluid mechanics is a branch of science and engineering which addresses the study of the properties and behavior of fluids, where gas or liquid phase materials are treated as fluids. Specifically, the field of fluid dynamics applies only to the study of the motion of fluids, formerly known as hydrodynamics. The terminology of the field has shifted somewhat over the past centuries, however, so that each term can be applied to the same general study of fluid behavior depending on the circumstance.

Regardless of the name applied, these methods traditionally describe properties and behavior of fluids from a continuum point of view, based on aggregate quantities which are averaged over the volume of the fluid contained within a differential fluid element. Density, viscosity, surface tension, and pressure are examples of fluid properties which define, given a set of boundary conditions, the way a fluid behaves at the continuum scale. The Navier-Stokes equations for fluid motion derive the behavior of a fluid from the sum of a viscous and pressure term, resulting in a stress on a differential fluid element. These equations yield three dimensional velocity data for that element. Though it has yet to be proven that a continuous solution to these equations always exists, they are nonetheless the definitive equations of motion when studying continuum dynamics of a fluid.

To help characterize the flow regime of fluids, certain dimensionless quantities have been developed. These dimensionless terms do not define a fluid, but instead describe the state of a fluid under a given set of conditions as a ratio of certain forces. The Reynolds number, for instance, is perhaps the best known of these quantities; it characterizes the ratio of inertial to viscous forces in a fluid at a certain point. It is given as

$$Re=\frac{\rho\, v\, L}{\mu} \tag{1}$$

where ρ, v, μ, and L are fluid density, velocity, viscosity, and characteristic length of fluid travel for a particular flow, respectively. The Weber number is another dimensionless parameter, relating inertia to surface tension, and it proves especially useful in the characterization of fluid interfaces; it is given as

$$We=\frac{\rho\, v^2 L}{\sigma} \tag{2}$$

with σ being surface tension at the interface. Regardless of the forces in consideration, these parameters are extremely useful in relating flow regimes of fluids because they describe an overall fluid condition, regardless of fluid type or properties. Essentially, flow characteristics and fluid properties are normalized by these quantities, providing the ability to compare two different flow scenarios even for different fluids. For example, if the appropriate dimensionless numbers of two different fluid flows are equal, those flows can be treated as equivalent and descriptions and characterizations applicable to one can be appropriately applied to the other.

Though bulk fluid properties and dimensionless parameters have gone a long way towards describing the majority of fluid flow regimes and fluid-fluid interactions, they have been observed to show certain limitations in their applications to fluid-solid interfaces. This is not so much true in the interaction of a static, continuous fluid-solid interface, but instead is problematic in the presence of a dynamic interface between the two. Such a case arises, for instance, in the case of a fluid drop on a solid surface. In this case, surface tension at the triple contact line (ie. the three phase intersection of the ambient vapor and drop fluid interface, drop fluid and solid interface, and ambient fluid and solid interface) creates unique problems for traditional fluid mechanics descriptions [1]. Equation (3) is one such description of the behavior of a fluid at an interface—the Young-Laplace equation. It describes the pressure difference Δp that exists across a fluid-solid interface in a circular capillary tube as

$$\Delta p=\frac{2\gamma}{R} \tag{3}$$

where γ is the wall or surface tension, and R is the radius of the spherical meniscus. Figure 1.1 shows a two-dimensional schematic of a prototypical drop on a wall at hydrodynamic equilibrium, with universal geometric features such as radius R, contact line L_c, and equilibrium contact angle θ_e denoted.

The contact line represents the line of intersection between the ambient fluid, drop liquid, and solid surface, whereas the contact angle θ is the angle formed between the line projected tangent to the drop at the contact line and the solid surface, as measured from the drop's interior. The radius is a measure of the distance between the centerline of the drop and the contact line. Note that the term contact line is somewhat misleading—for an initially spherical drop spread uniformly on a flat surface, the contact "line" will be circular. However, for one-dimensional wetting (for a liquid line spreading perpendicular to the line direction), the contact line is actually linear. Despite this, even the circular three phase contact region is commonly called the contact line. Considering the length scale of a fluid's constituent atoms or molecules compared to the length scale of a macroscopic drop's contact line, it can be concluded that fundamental atomic scale mechanisms of drop wetting are not influenced by macroscopic curvature of the contact line. In other words, at the atomic scale, the local three phase contact region is effectively linear. This may break down for sufficiently small drops when the curvature of the contact line approaches the nanoscale. However, herein, the contact line nomenclature is adopted.

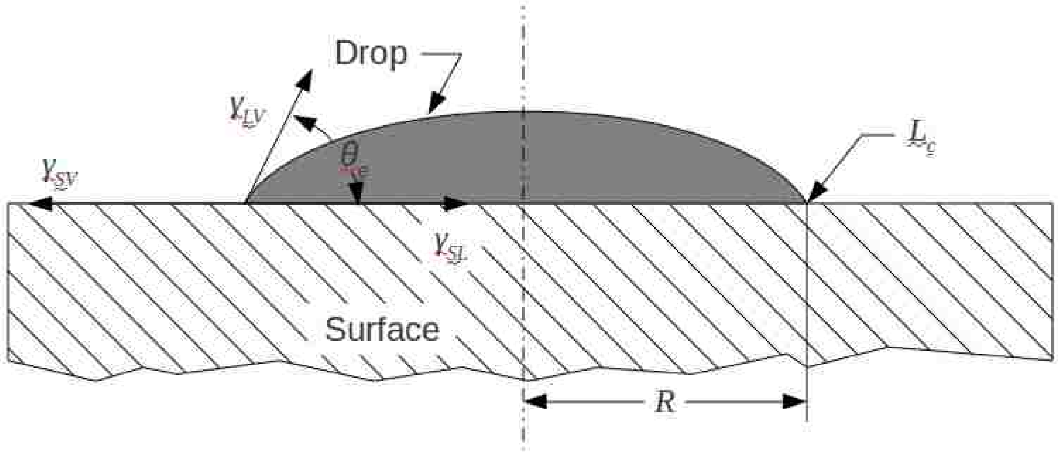

Figure 1.1 Schematic of a liquid drop on a solid surface at equilibrium.

This introduces the concept of wetting, which can be defined as the process by which a fluid covers a surface. It typically involves the displacement of one fluid by another, as in the case presented above where the ambient vapor is displaced by the liquid drop [2]. The first quantitative development to characterize thermodynamics of a wetting system was advanced over 200 years ago and is represented by the Thomas Young equation:

$$\gamma_{LV}\cos\theta_e+\gamma_{SL}-\gamma_{SV}=0 \tag{4a}$$

or

$$\cos\theta_e=\frac{\gamma_{SV}-\gamma_{SL}}{\gamma_{LV}} \quad . \tag{4b}$$

This effectively represents an energy balance as γ_{LV}, γ_{SL}, and γ_{SV} are the interfacial energy of the liquid/vapor, solid/liquid, and solid/vapor interfaces, respectively. As depicted in Figure 1.1, Young envisioned each interfacial energy term as a driving force to either promote or resist contact line advancement [3]. For instance, in the limit where either or both of γ_{LV} and γ_{SL} are large relative to γ_{SV}, the drop is driven towards a relatively larger θ_e. Thus it can be seen above that θ_e characterizes the thermodynamics of a wetting system.

1.2 Introduction to wetting

Wetting is a ubiquitous phenomena that is present not only in every day activities, but also forms an integral part of many engineering processes. Painting and spray deposition of coatings are two general examples of such processes. Despite its widespread presence, the fundamentals and intricacies of the wetted interface are still largely poorly understood. It is generally understood that the dissipation of surface free energy drives the spreading of liquids. The mechanisms of this dissipation, however, are still a matter of scientific debate [2].

At this point a distinction must be made between the two types of wetting that might occur on a solid surface: full and partial. The schematic in Figure 1.1 depicts partial wetting by the drop, where the contact angle is in the range $0^\circ < \theta_e < 180^\circ$. Full wetting only occurs in the case where the fluid contact angle nears the limit $\theta_e \rightarrow 0^\circ$. Figure 1.2 shows the difference between the two, though it can be understood that any system involving a singular drop on a solid interface will fall within the partial wetting category [1].

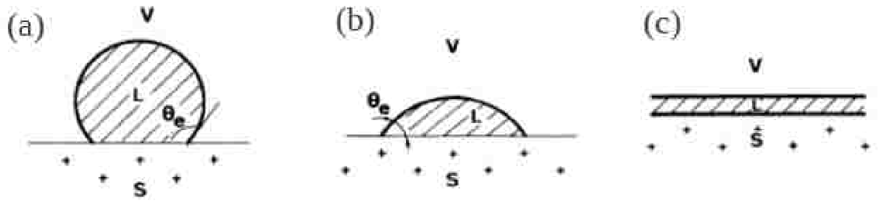

Figure 1.2 Equilibrium contact angles, θ_e, for two partially wetting drops (a) and (b), and one fully wetting drop (c). V, L, and S denote vapor, liquid, and solid respectively. Note that the drop in (a) is sometimes referred to as a "non-wetting" drop defined by $90^\circ < \theta_e < 180^\circ$ [1]. Charges depicted in the solid are purely schematic; the situation is the same for non-ionic solids.

Wetting and spreading, it must be noted, are subtly different terms both used in describing wetting phenomena; wetting has been defined earlier as the process in which a liquid covers a surface, while spreading is more loosely used as a description of the motion of the drop as it moves towards equilibrium on the surface. Given a smooth uniform surface, a wetting drop will ideally form a spherical cap with a circular contact line at equilibrium; thus, the radius of the contact area can be used to characterize the degree to which the drop wets the surface. However, this will scale with initial drop size. To remove dependence on drop size, the equilibrium contact angle is more often used as a means of parameterizing how well a liquid will wet a surface.

When a drop is initially brought into contact with a solid surface, the contact angle is 180˚ and the radius of the wetted region R is zero. To reach equilibrium, the drop spontaneously spreads on the surface such that θ decreases from 180˚ to θ_e. In this process, R will increase until the system reaches equilibrium. The value of R at equilibrium is dictated by the starting drop volume in connection with θ_e. Because wetting and spreading represent phenomena by which a system approaches equilibrium, it is of interest to characterize the kinetics of wetting. For the drop geometry described above, it can be seen that the time dependence of the contact angle, $\theta(t)$, and the time dependence of the radius of the wetted region, $R(t)$, are suitable metrics for characterizing wetting and spreading kinetics.

1.2.1 Wetting characterizations

Some mention has already been given to the way in which a drop spreads dynamically over the surface. Hydrodynamic equilibrium and surface tension have been presented briefly in describing a drop's equilibrium shape, but these only generally describe the mechanisms driving spreading behavior. Specifically the drop is out of equilibrium while it is spreading, and the degree to which it is out of equilibrium drives this spreading. In an effort to precisely describe the non-equilibrium kinetics of wetting, scientists have developed mathematical models which predict the way a liquid drop will behave. These models focus on $R(t)$ and $\theta(t)$ during the spreading process; relationships to describe $R(t)$ and $\theta(t)$ are derived based on fundamental assumptions of the dominant energy dissipation methods at work within the fluid system. Given the volume of liquid in a spreading drop and an assumed shape for the drop (ie. a spherical cap), note that an expression for $R(t)$ can be derived from an expression for $\theta(t)$ given simple geometric considerations.

The original and historically most natural descriptions of wetting have grown out of classical fluid mechanics. Hydrodynamic (HD) wetting theory, as it is simply known, assumes viscous dissipation of kinetic energy as the dominant mechanism dictating liquid wetting kinetics. Expressions derived via hydrodynamic wetting theory describe $R(t)$ (and $\theta(t)$) in terms of the viscosity of the spreading liquid. A model of spreading was developed for the case of a cylindrical drop and presented by Heine, et al.; a similar presentation can be made for a spherical drop but a cylindrical case is presented here. This case shows that the time derivative of radius of the drop can be expressed as

$$\frac{dR}{dt}=\left(\frac{A}{\theta-\sin\theta\cos\theta}\right)^{1/2}\left(\cos\theta-\frac{\sin^3\theta}{\theta-\sin\theta\cos\theta}\right)\frac{d\theta}{dt} \tag{5}$$

where A is the area of the circular segment defined as $A = 1/2\, R^2\,(2\theta - \sin 2\theta)$. The change in free energy of the drop is determined by integrating the surface tensions at the three interfaces, which yields

$$\frac{\partial F\{r(t)\}}{\partial r(t)}=2L\gamma\left(\frac{\theta}{\sin\theta}-\frac{\theta_0}{\sin\theta_0}\right) \tag{6}$$

with *L* representing the length of the cylindrical drop for this derivation. Based on the mechanical description of dissipative system dynamics, the dissipation function *Γ* can be represented as

$$\frac{\partial \Gamma\{R(t);\dot{R}(t)\}}{\partial \dot{R}(t)}=\frac{\partial F\{R(t)\}}{\partial R(t)} \quad . \tag{7}$$

The dissipation function is composed of a kinetic and hydrodynamic component; the kinetic term results from molecular adsorption near the contact line, while the hydrodynamic term is derived from the solution to equations of motion and continuity. At the limit where dissipation is due to hydrodynamic effects, the hydrodynamic model applies, and at the limit where dissipation is due entirely to molecular kinetic effects, molecular kinetic theory is applicable. Heine's model, as presented previously for cylindrical drops, is a combined model. The derivation of a cylindrical drop description is more directly compared to our wetting studies presented herein, which are also based on simulations of cylindrical drop wetting. Kinetics predicted by such a model can be bounded by considering the molecular-kinetic (MK) versus hydrodynamic limits. Originally developed for a spherical drop, Blake's molecular-kinetic model predicts $R(t)$ dependence of $t^{1/7}$, and Tanner's hydrodynamic model predicts radial growth dependence as $t^{1/10}$. Heine, et al. then showed that these scale to describe the radial expansion of a cylindrical drop as $R(t)\propto t^{1/5}$ for the kinetic model and $R(t)\propto t^{1/7}$ for the hydrodynamic model [4].

Tanner's model represents the effective limit of hydrodynamic theory for wetting. Liquids behaving outside of this envelope (ie. those spreading more rapidly than predicted by hydrodynamic theory) are said to exceed the “hydrodynamic limit” and thus can not be accurately described within hydrodynamic theory. Many relatively “fast spreading” liquids, for instance, do not fit this model and have prompted re-evaluations of wetting phenomena and driving mechanisms. Examples of liquids that spread outside the hydrodynamic limit are water on hydrophilic surfaces as well as a number of small molecule polymeric liquids on inert surfaces.

Molecular kinetic theory (MKT) represents the major alternative to classical hydrodynamic theory. Instead of treating liquid viscosity as the primary dissipation mechanism, this model treats the fluid-solid interaction as the primary source of energy loss in the spreading liquid. Somewhat sacrificing the no-slip boundary condition of hydrodynamic theory for a “surface friction” term, MKT treats the advancement of the contact line as a stepwise motion defined by liquid molecule “hopping” across the surface from one low energy adsorption site to an adjacent one. Energy dissipation occurs as capillary pressure from the liquid drives molecules (or atoms) at the contact line from one potential energy minimum at the surface to the next; to accomplish a site to site hop, an atom or molecule must overcome an energy barrier. This barrier is the mechanism behind the surface friction term and it manifests energy dissipation. Spreading ceases when the capillary pressure on the particles at the contact line is no longer great enough to force them over the next potential energy barrier. Figure 1.3 presents a conceptual schematic of this advancement.

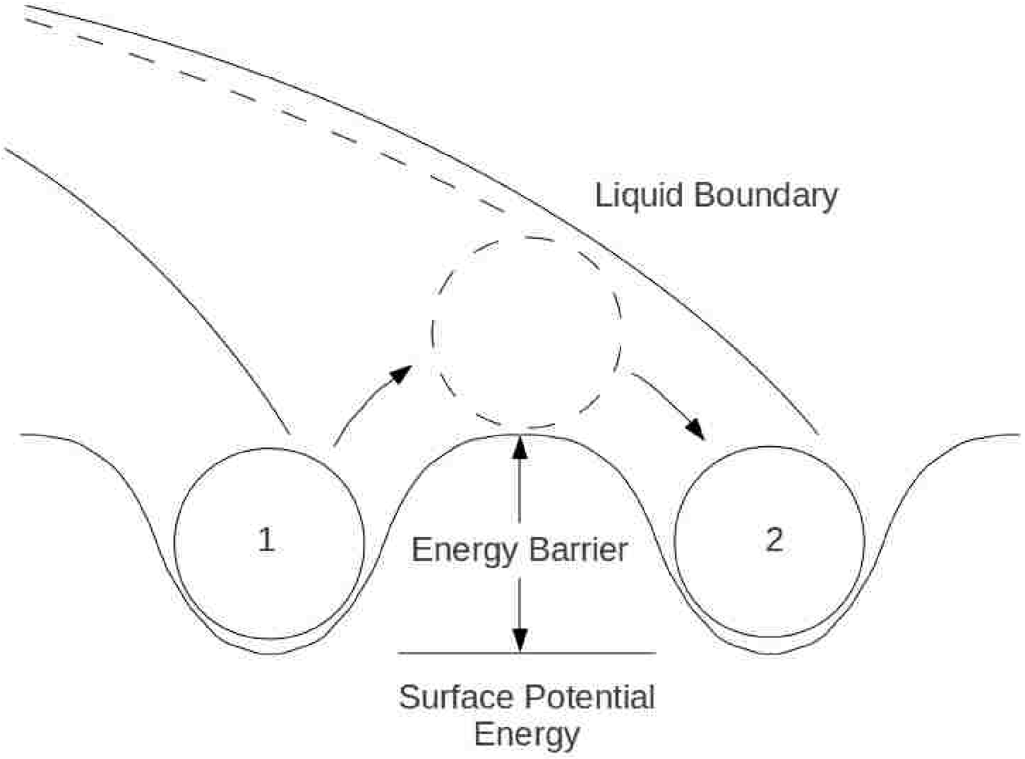

Figure 1.3 Conceptualized representation of molecular kinetic model of contact line advancement. The atom initially in position 1 moves to position 2 by overcoming a potential energy barrier. This advances the contact line.

Despite the fundamental difference in the basis for the theory, molecular kinetics still seeks to predict the behavior of a wetting liquid by radius and contact angle change as a function of time. Blake's relationship is commonly invoked to describe molecular-kinetic radial advancement, as explained previously. Similar to hydrodynamic theory, spreading regimes can be observed which do not fit the molecular kinetic model, while still falling outside of the hydrodynamic limit. To describe kinetics for such cases, hybrid theory incorporating both models has also been advanced and shown to overcome limitations exhibited by HD and MK theories alone. However, cases still exist for which hybrid models can not describe the system's wetting dynamics very well.

An example of systems where wetting kinetics are not well described by HD theory, MK theory, or even hybrid models are so-called reactive wetting systems, where significant chemical reactions occur between solid and liquid. Wetting theories so far presented assume an inert solid, so it is not surprising that they exhibit deficiencies when describing kinetics in systems for which this assumption is strongly violated [6-11].

Water spreading on glass at room temperature, for instance, is completely nonreactive wetting that is well described by a hydrodynamic model, while water spreading on a sugar cube represents a reactive wetting scenario for which hydrodynamics and molecular kinetics are poorly suited. Even reactive systems do not all behave the same, as certain reactions are localized to the interfacial region and others involve a relatively large portion of the surface material on the order of the initial volume of the drop. High temperature wetting systems typically fall into the category of reactive wetting, and their study requires the application of a more sophisticated model to identify the dominant mechanism of fluid transport. High temperature is a relative description that is typically invoked to characterize systems for which melting occurs well above room temperature; thus, it is a term often used to describe wetting for liquid metals and ceramics.

An example of a high temperature wetting system is Si wetting graphite. For this system, a drop initially brought into contact with graphite rapidly spreads from a contact angle of 180˚ to a smaller, but still relatively large contact angle of ~ 130˚. At this point, wetting slows dramatically, nearly seeming to halt. However, the Si(*l*) reacts with the substrate to form silicon carbide, SiC, which is wet better by the liquid Si than is unreacted graphitic carbon. Here again, better wetting is taken to mean that the liquid spreads to a lower contact angle on the surface. SiC formation is localized to a thin reaction layer at the solid/liquid interface and the progression of Si across the surface due to the carbide formation is relatively slow compared to the initial wetting of the graphite. In this situation, spreading kinetics are limited by the rate of the carbide formation reaction. The example of water on sugar, however, is a reactive wetting scenario where the reaction is not localized to a thin layer. Instead, in this situation, the substrate dissolves into the liquid; water will absorb sugar to the point of saturation. Figure 1.4 depicts two differing reactive wetting systems in schematic form. The distinction of the type of reaction is critical to the description of the wetting behavior of the two systems.

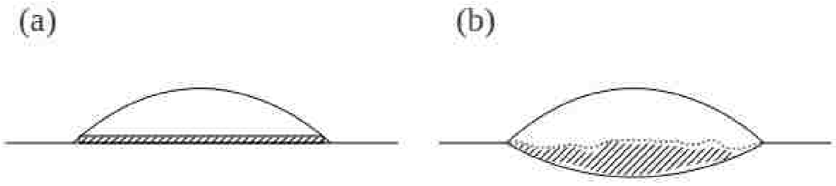

Figure 1.4 Cross sections of reactive wetting systems. In (a) the reaction between solid and liquid is constrained to a thin layer at the interface, whereas in (b) the reacted zone extends more significantly away from the solid/liquid interface. Hatching represents the reacted areas between liquid and solid.

Reactive wetting theories address wetting in terms of the type of reaction manifest at the solid/liquid interface. As before with nonreactive wetting models, reactive wetting models attempt to explain observed kinetics in terms of dominant dissipation mechanisms. The difference for reactive wetting models is that dissipation is assumed to be directly connected to mechanisms of the relevant reaction. Three main classes of reactive wetting systems have been identified. In one class, the rate of the reaction at the solid/liquid interface is assumed to limit spreading kinetics. Models describing such interface limited, or reaction limited, spreading predict $R(t)$ is linear:

$$R(t) \propto t \quad . \tag{8}$$

Indeed some high temperature systems, like Si(l) on graphite, exhibit linear regimes in $R(t)$. Another class of reactive wetting models assumed spreading kinetics are limited by the rate of transport of reactants to the reaction zone. In so-called diffusion limited reactive wetting, models predict

$$R(t) \propto t^{1/4} \quad . \tag{9}$$

The system of a sessile NiSi drop reactively wetting porous graphite, for example, exhibits regimes in R(t) that agree reasonably well with the $t^{1/4}$ dependence [7-9].

The earlier example of water wetting sugar represents a third class of dissolutive reactive wetting. This is also what is seen when Ag(l) wets Cu or when Cu(l) wets Ni [11,12]. For any system where a high degree of solubility exists for the solid in the liquid, in fact, dissolutive wetting occurs. In such instances, simulations and experiments give evidence that

$$R(t) \propto t^{1/2} \quad . \tag{10}$$

However, mechanisms responsible for the $t^{1/2}$ dependence are unknown. Interestingly, most partially or fully wetting systems—reactive or not—exhibit a very early time behavior where $R(t)$ increases proportionally as $t^{1/2}$. This regime is referred to as the inertial spreading stage, when the drop moves from the highly non-equilibrium initial contact angle of ~ 180° to a lower, but still non-equilibrium, contact angle. The inertial spreading stage $t^{1/2}$ dependence is observed in a wide variety of wetting systems, regardless of reactivity. However, this is not as surprising as it first seems—the inertial spreading stage is constrained to very early time, essentially before reactions noticeably impact kinetics. This fairly universal inertial spreading regime therefore seems to emerge as a response to the highly non-equilibrium initial state when a drop contacts a solid surface. It is proposed to arise during the time when non-constant curvature exists in the liquid/vapor interface. It is generally held that the dominant dissipation mechanisms are similar to those dictating surface diffusion, thus the dependence on $t^{1/2}$. However, the cause of the similarity between time dependence during inertial wetting versus dissolutive wetting remains an unknown. In the latter case, activity is clearly not restrained to atomic transport across a surface. Instead, the diffusive-like kinetics exhibited in dissolutive wetting systems may result from the rapid production of new liquid and the associated diffusion fields that develop to bring the spreading liquid to chemical composition homogeneity.

These reactive wetting descriptions are idealizations, and the true behavior of reactive wetting systems can be far more complicated. In the cases noted above, the drop is assumed to be introduced to the surface at negligible velocity, so that spreading kinetics are driven solely by capillarity (and reaction rate, where appropriate). Such drops are referred to as having a sessile configuration, and differ from “kinetic” drops—

which have non-zero impact velocity—in terms of wetting behavior. Sessile drops are useful for theoretical study because of their exclusion of significant momentum effects on a wetting drop, but because of this, are not completely analogous to liquid wetting seen in most industrial processes, for instance.

The cases noted above are also completely isothermal models, where liquid and solid properties are well defined and remain so throughout wetting in the absence of chemical reactions. These assumptions are challenged in real wetting applications; indeed, many wetting problems involve an imperfect fluid contacting an imperfect surface under non-isothermal conditions. Thus, fundamental fluid and solid properties may not be well defined or may vary spatially or temporally. Many applications involve drops contacting a solid with non-zero approach velocity, as noted earlier. Thermal spray processes, for example, often involve highly reactive wetting of a high temperature molten metal drop on a relatively cool metallic surface, where the drop is made to impact the solid surface at high velocity. Such wetting regimes demand more rigorous investigation into relevant dissipation mechanisms, and further explanation of thermal spray processes and simulation of reactive wetting will be presented later in this chapter.

1.3 Wetting applications

As stated previously, wetting has widespread engineering applications. The wetting and solidification of materials onto surfaces under the broad category of coatings is one of these important fields of application. Within the context of coating processes, application of the coating material is usually carried out through the deposition of liquid particles, known as drops, onto solid surfaces, or substrates. Lubrication, airbrushing, ink jet printing, and an entire industry dedicated to metallic, oxide, and ceramic coating procedures rely directly on this wetting process. Metallic coatings in particular take on an array of roles, from thermal barrier coatings to semiconductor manufacturing. Improvement of surface properties of the substrate is achieved and, in the case of semiconductor manufacture or printing, key features of the finished product such as microcircuit features are created entirely by means of the coating [13-20].

1.3.1 Thermal spray coatings

Thermal barrier coatings are important in the propulsion and energy generation sectors; combustion processes benefit from improved efficiency under steady, high temperature operation. Operating conditions routinely in excess of the melting point of iron make component durability of key importance—failure of a part in a gas turbine, for instance, can not only be costly to repair, but dangerous and catastrophic especially in aerial propulsion settings. Wear resistance and improved thermal conductivity of the substrate surface, therefore, are two highly desirable characteristics of most metal coatings. The quality of these properties thus relies directly on the adhesion and surface condition of the coating on the substrate. Specifically, thermal spraying of metals, or “flame spraying” as it is often (though somewhat imprecisely) referred to, is a well-established industrial process for metal deposition that, under the proper conditions, produces such coatings. Ceramics or other highly refractory materials, as well as polymers, are also widely applied by thermal spraying.

1.3.2 Features of thermal spray deposition

To examine the thermal spray process, it is useful to first understand the conditions of the drop and substrate typically seen in industry from a process operator's or experimentalist's point of view. Thermal spray is unique in that most of the complicating factors possible in wetting studies are present and play an important role in governing the spreading dynamics and final drop morphology. First and foremost, the liquid being deposited is typically a metal or metal oxide. Such materials typically require significant heating to become molten for spraying, and thus their drops begin at a high initial temperature. Due to the high thermal conductivity of metals, conditions also exist for significant transient cooling of the molten drop. Conduction to the surrounding atmosphere during travel to the substrate, as well as to the substrate upon impact, can rapidly or slowly quench the drop. Atmospheric conditions can vary widely from air to inert gases, potentially at varying pressures. Alloying in both the metal drop and surface can complicate the fluid properties of the metals while molten. They also dictate the properties of the system at impact, potentially complicating their interaction in a wetting process that is, due to the high temperature gradient, highly reactive. Whereas many wetting processes feature relatively negligible impact velocities, thermal spray deposition features high drop velocity, with the additional possibility of physically deforming the substrate surface due purely to kinetic energy on top of the necessary deformation due to conduction and mixing between drop and surface. Upon impact, the surface texture and chemical composition of the substrate necessarily dictate the system's behavior. Mixing and exposure to the ambient atmosphere can lead to a change in the chemical composition of both substrate and drop over the course of the splat formation, as well.

Finally, and most importantly, typical thermal spray drops are on the order of microscopic scale. This means that the total time for splat formation and solidification are equally small due to rapid conductive cooling. Capturing the impact of microscopic drops impacting imperfect surfaces in the span of microseconds poses currently insurmountable problems to experimental capabilities. Gaining insight into the dynamics of the splat formation beneath the outside of the drop is physically impossible as well. Visual inspection of the splat formed after solidification is possible to investigate the final state of the splat and substrate; however, visual methods can not be used to penetrate the molten metal drop during splat formation. Even the examination of a single drop impact is possible, but has proven extremely difficult to produce experimentally. Most such experiments are executed on isothermal systems at room temperature (ie. low melting point liquids).

1.3.3 Thermal spray applications

Dipping, vapor deposition and thermal spraying are three established families of coating methods. The term “flame spray” or “plasma spray” is often times associated with the class of manufacturing techniques technically known as thermal spray coating (indeed, flame and plasma spraying are themselves two particular types of thermal spraying each with their own distinguishing features). Thermal spraying, then, is a class of processes for the coating of surfaces to lend protection against environmental attack.

The essential requirements for coatings are:

- Excellent environmental resistance
- Long term protective operating life of the coating
- Strong adhesion to the coated surface

High temperature corrosion resistance in metal components is achieved through the creation of a protective layer on the substrate's surface. This layer must be inert in and impervious to the environment, which is made difficult at high temperatures because of the extreme reactivity of the environment with metals in such conditions. Ceramics, oxides, and dissimilar metals can be applied to the substrate material to achieve these ends, depending on operating conditions [13,21].

Thermal spray coatings heat a feedstock material and project it onto a surface typically by means of a forced gas or plasma jet. Typically feedstock materials are powders or wires. The feedstock is converted to discrete particles, either before being fed into the thermal spray apparatus or through the heating and spraying process itself. Ideally, each particle becomes fully molten before contact with the surface. Dozens of variations on this basic definition have been developed in the past century since Schoop demonstrated the first recorded flame spray process in 1917. Different classes of thermal spray techniques, each encompassing a number of specific processes, have formed around a few key characteristics.

One such thermal spray class is characterized by particles possessing high kinetic energy in contact with jets or flames with high velocity but relatively low temperature to avoid unwanted reactions. Travel distance of the particles to the surface is usually small, and coating materials usually have relatively low melting points compared to the melting points of materials used in other classes of thermal spray processes (not compared to standard atmospheric temperature). Materials which undergo modification of their chemical composition during spraying, such as carbides which decarburize, are frequently applied through such methods. Another class of thermal spray is distinguished by a controlled atmosphere surrounding the jet or flame at spraying. In such processes, the environment surrounding the particle stream is not air at atmospheric pressure. This protects the coating and substrate from oxidation or alters the effective fluid dynamics of the jet stream itself. Such processes are used for the deposition of materials with high chemical affinity to oxygen or those which are intended to form coatings without oxides. Still other coating techniques are designed for high productivity; low quality, high volume applications such as the application of metals or alloys (ie. Mo, Ni, NiCr, NiAl) to large surfaces benefit from large coating material throughput, as do certain high performance oxide coatings (Cr_2O_3 or Al_2O_3, for example) which are also applied on large surfaces. Finally, nanostructure particle coatings are now routinely applied via an emerging class of thermal spray techniques which enable the formation of crystal grains in the coating layer at the sub-micrometer scale. Processes in this class are typically modifications of existing ones which allow for the size of the particle (and the resulting coating thickness) to be kept small.

Because there exists such a wide array of materials employed as coatings in flame spray, the processes are classified by the method through which they deposit coating material to the substrate. These include, but are not limited to: flame spraying, atmospheric plasma spraying, arc spraying, detonation gun spraying, vacuum plasma spraying, and cold gas spraying.

Before explaining specific thermal spray types and their interesting applications in connection with this paper, however, surface treatment should be mentioned. Surface pretreatment is a critically important first consideration regardless of thermal spray technique. The substrate surface must first be cleaned to remove any protective coatings or oxide layers, and then “activated” to promote adhesion. Activation is frequently accomplished by grit blasting, laser ablation, or chemical treatments when appropriate. Numerous studies have been dedicated to the topic of substrate topography effects on coating adhesion and, indeed, on wetting behavior in the macroscale. The effects of surface topography on thermal spray coatings, and wetting in general, are extensive; indeed, they represent an area of study within wetting and coating research on their own. However, as will be discussed further in subsequent chapters, it is reasonable to consider uniform planar surfaces as a starting point for more fundamental studies of wetting behavior, without complicating geometric factors taken into consideration.

Subsequent to coating, surface post treatment is usually performed. Post treatment is, like pretreatment, a critical and widely varied process which can greatly improve the performance of a coating from the as-sprayed state. Classic examples include heat treatment, laser surface glazing, and chemical impregnation. Heat treatments, for example, can be carried out through electromagnetic heating, furnace treatment, or combustion flame treatment. Heat treatments are particularly applicable to metallic coatings. They can improve the adhesion between coating and substrate or enhance mechanical properties in the coating layer. They can also alter the chemical composition of the coating, such as driving out oxides, depending on atmospheric conditions within the furnace. An example of this is in vacuum furnace heat treatment used for improving adhesion of bond coatings in the application of thermal barrier coatings (TBCs) to gas turbine blades. Newer techniques such as laser processing have emerged over the past decade and not only bring their own suite of coating improvements, but also have introduced equipment that has improved upon established techniques. Laser treatments, for example, have begun to be used to improve the quality of biomedical, thermal barrier, and wear-resistant coatings (anilox rolls, for example, benefit from the precision of laser surface treatments) [6].

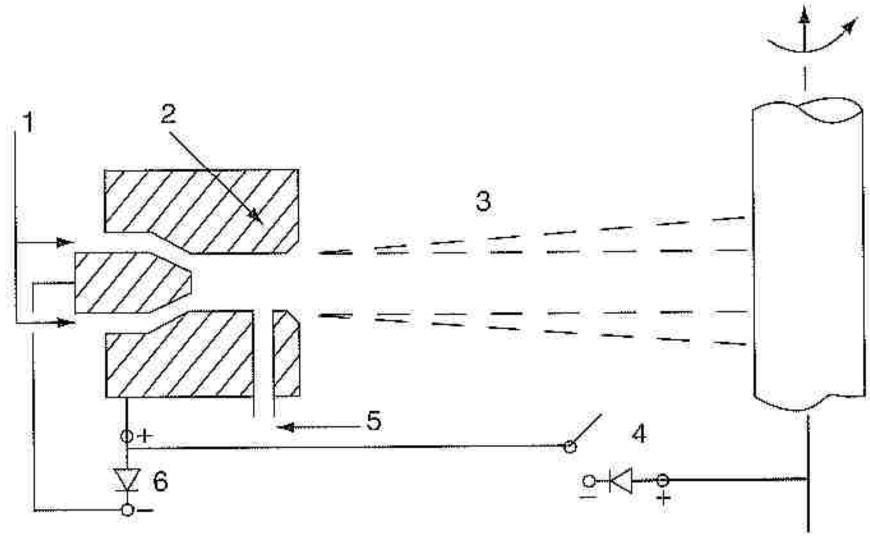

Figure 1.5 A schematic of a vacuum plasma spray (VPS) apparatus. The substrate is represented as a spinning shaft to the right. Parts labeled represent (1) working gas inlet, (2) the anode, (3) vacuum spray environment, (4) the arc generator, (5) powder inlet, and (6) the plasma generator [13].

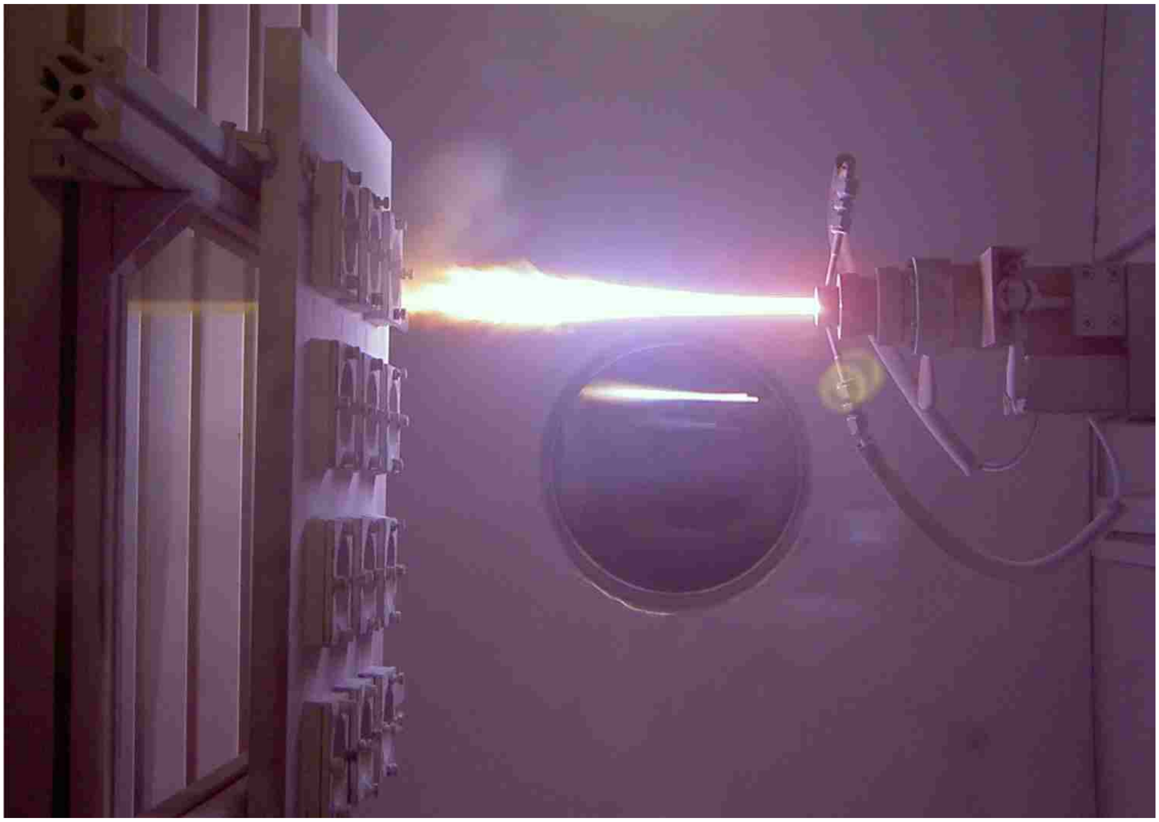

Figure 1.6 Example of a VPS process at the Institute of Technical Thermodynamics, German Aerospace Center (Zepper, 2004).

There are a few methods which experience approximately similar operating conditions to those simulated for the study in this paper: detonation gun (D-gun), high-velocity oxy-fuel (HVOF), and Vacuum Plasma Spraying (VPS). D-gun and HVOF are similar processes which heat and accelerate coating particles in a tube via combustion of fuel and oxygen behind the powder in the tube. They produce high quality coatings which have largely replaced electrolytic chromium in the aerospace industry with carbide reinforced composites and metal alloy coatings. VPS uses an electric plasma arc to heat and accelerate particles through a nozzle and uses an additional arc to either heat or clean the surface of the substrate. A schematic of the VPS process is given in Figure 1.5;

though not identical to the other thermal spray processes mentioned above, it is the process that is most closely simulated by the wetting studies which will be presented herein. A picture of an actual VPS setup is shown in Figure 1.6. It is used in the application of hot corrosion resistant TBCs for turbine blades and pure copper coatings for the electronics industry. Low pressure VPS represents a more economical alternative to vapor deposition techniques for creating very thin (below 50 μm) coatings for electronics. Table 1 presents approximate coating properties for these techniques, with an emphasis on the particle conditions. All three of these techniques are capable of delivering coating porosity below 1 % with average tensile bond strengths between 60 and 90 MPa [13].

Table 1. Coating properties for selected thermal spray processes [6].

Spray technique	Particle velocity (m/s)	Particle size (μm)	Coating thickness (μm)	Spray atmosphere
D-gun	750 - 3000	5 - 60	< 300	Atmospheric air
HVOF	1000 - 3000	5 - 45	< 300	Atmospheric air
VPS	1500 - 3500	5 - 20	< 50 - 500	Low vacuum air

1.4 Single drop wetting experiments

Single drop wetting analysis is useful not so much in how it replicates actual flame spray processes, but moreso in understanding the mechanisms of dissipation within a flame sprayed drop on a theoretical fundamental basis. Single drop wetting experiments, such as those conducted by Li, et al. [22], allow for the detailed observation and quantification of individual drop wetting behavior in regimes similar to those observed in thermal spray procedures. Drop morphology was studied, and the relationship between Reynolds number and flattening of the drop on a substrate was analyzed. The experiments also involved the preheating of the substrate, based on the observation that preheating the surface below its melting point inhibits the formation of splashing during molten drop spreading. Tests conducted using molten Cu(*l*) drops projected onto stainless steel via plasma spraying in ambient air yielded results agreeing with the relation

$$\psi = 1.21\, Re^{0.125} \tag{11}$$

where ψ is the flattening degree and Re the Reynolds number. The flattening degree is the ratio of the solidified drop diameter to the original molten drop diameter D_{SOLID}/D_{DROP}.

The paper acknowledges three mechanisms as determining the final drop size: viscous and surface tension dissipations of inertial energy and the resistance to liquid flow by drop solidification. The last mechanism is of particular interest not only for the determination of the final drop radius, but in that it identifies a feature of reactive wetting behavior which non-reactive wetting experiments and simulations can not capture. As an experimental study, however, the evolution to final drop geometry is not observed in Li's work; the kinetic mechanisms of contact line advancement in a highly reactive wetting situation remain unresolved by experiments to date [22]. Numerical simulations thus offer the advantage of greater temporal and spatial analysis of wetting behavior over experimental apparati.

1.5 Analytical techniques for wetting study

Due to the aforementioned experimental difficulties in studying drop wetting during a typical flame spray process, simulations of molten metal drop wetting have also been investigated extensively in the past decade. Due to the evolution of affordable widespread high speed computing in recent years, researchers have taken advantage of a number of established numerical techniques to simulate drop impact and wetting behavior. Sessile geometry drops have been widely studied; the spreading of a sessile drop is driven primarily by the dissipation of surface free energy, as described earlier. This is opposed to kinetic impact geometries, in which the drop velocity is non-negligible at contact with the surface and in which the drop spreading is driven by momentum as well as surface energy dissipation. Temperature differences between the drop and surface is another distinction between wetting regimes; though mainly isothermal systems have been studied to date, systems involving non-isothermal drop and substrate and phase changes throughout the wetting process present another distinguishing feature between types of wetting simulations—one that is particularly relevant to wetting of drops in thermal spray processes.

Among the simulation techniques used to study wetting behavior—namely, Monte Carlo (MC), Phase Field, Volume of Fluid (VOF), Computational Fluid Dynamics (CFD), and Molecular Dynamics (MD) approaches—MD has proven useful in simulating wetting mechanisms at the atomic level. The advantages of MD over experimental and other numerical techniques center on its atomic scale spatial resolution along with continuous time trajectories of an atomic ensemble. In other words, very few assumptions need be made in building a model of a physical process. For example, the contact angle of a spreading drop need not be specified as an input; it is instead a result of an atomic scale model. The drawbacks of such a simulation technique, however, lay in its greatest advantages; the atomic scale and sub-nanosecond scale of the simulation means the simulation of even micrometer-sized drops over the course of tenths of a second is still a prohibitively demanding task. Bridging the gap between what is feasible to produce in MD and experimentally is still an important step for researchers to fully elucidate details of drop impact, wetting, cooling, phase change, and final morphology [23].

The implication of the precision of MD simulations, but the limited system size on which they can be applied, is that the study of wetting behavior using MD must be a multiscale one. Fundamental mechanisms can be observed from atomistic simulations, and mesoscale analogies can be used to bridge the gap to continuum scale where observations of such mechanisms can be applied to actual engineering processes. In this study, an atomic model of drop impact, spreading, cooling, and solidification is presented. Emphasis herein is on model development and preliminary results of simulations conducted with that model.

2. Numerical Simulation Techniques

2.1 Simulation motivation

While many complex physical phenomena are well defined by established theoretical models, such an understanding is not universal. Within the context of drop impact, wetting, and solidification, for instance, there still exist fundamental physical interactions which current theoretical models fail to accurately predict [1]. Experimental analysis techniques offer the promise of very high analog resolution in the data available, but often fall short in the actual collection of physical information. It is virtually impossible to examine physical phenomena deeper than the macroscopic level to elucidate fundamental mechanisms of contact line advancement in an experiment. This is a problem which manifests itself to varying degrees, depending on the scale and complexity of the system under examination, but is especially poignant in studies at the microscopic level. Actually capturing the information available in a system at such scales frequently proves so difficult that even sophisticated techniques are only able to record a few physical properties. In these cases, numerical simulations of the physical system in question can provide detailed information unavailable to the experimentalist alone. It is desirable to utilize a simulation technique that specifically reveals the behavior elusive to experimentalists in studying dissipation mechanisms of wetting.

This is not to say, however, that numerical simulations can supplant experimental data entirely. Simulations must be closely parameterized with information about the system, and this data must come either from theoretical derivations or experiments.

Experimental data is in this way usually the point of origin of any simulation, as the model developed from that data forms the input parameters for simulations of similar systems. Simulations can be used to predict the outcomes of experiments as well as for validation of theoretical models without the introduction of simplifying approximations (see Figure 2.1). Thus, numerical simulations are not just an important tool; it can be argued that they represent an important field of science. Indeed, many researchers now consider computational simulation as a third pillar of scientific inquiry in its own right alongside the more established pillars of experiment and theory.

Simulations are tools used by scientists to replicate physical systems by means of the application of a model of that system in a numerical algorithm. The accuracy of any simulation is dependent upon the integrity of the model on which it operates, and the simulation itself is a bridge by which scientists can span between reality and a model, learning details about the physical system by the careful study of the behavior of its model under controlled conditions. The sheer diversity of phenomena existing in all of the physical world, and indeed the universe, has lead researchers to develop correspondingly diverse and numerous simulation techniques for the detailed study of these phenomena. Less generally, numerical simulations of physical systems are used in place of experimentation, to provide information regarding phenomena not easily obtained in an experimental setting. The study of liquid drop impact and wetting behavior, for instance, has benefited from the improved insight which numerical simulation techniques offer.

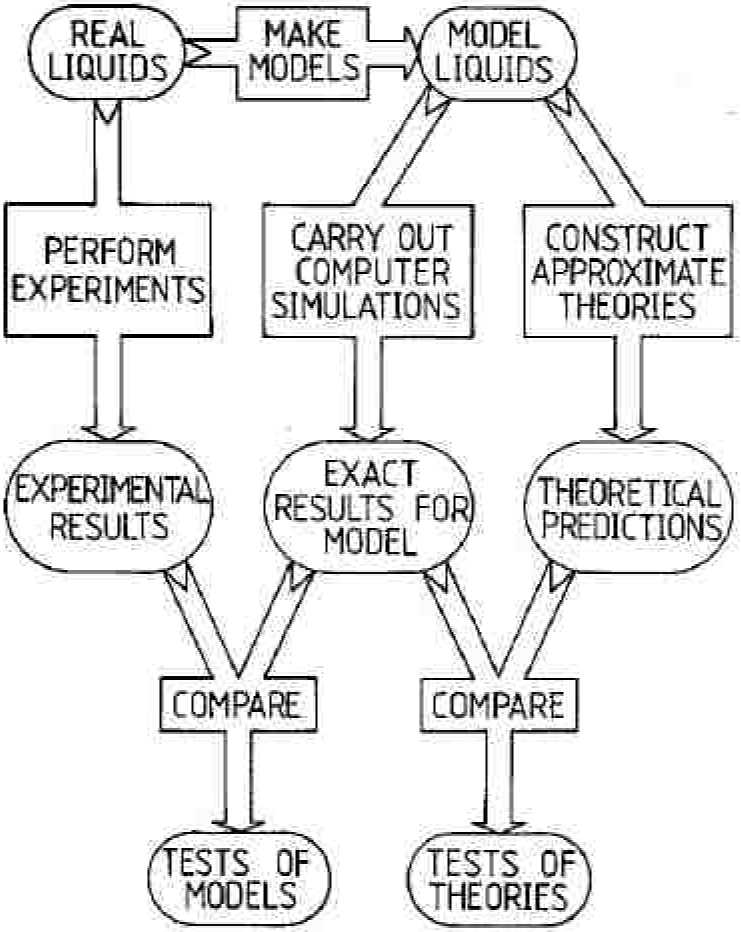

Figure 2.1 Schematic representation of the relationship between experiment, theory, and simulation [23].

A natural way to classify the various simulation techniques is by the length and time scales accessible to them. Again, simulations are only as accurate as the models on which they are based, and thus the time and length scales inherent to the model dictate the scope of the technique which uses it. Figure 2.2 shows a diagram of approximate time and length scales accessible by different simulation method types.

Quantum simulations must be used when electronic degrees of freedom are significant in a system. For example, if atomic bond strength is to be computed, quantum mechanical methods must be brought to bear. Because of electron resolution, length and time scales are very small for quantum simulations. Classical MD potentials represent atoms as point-wise particles and thus do not actually resolve electronic degrees of freedom. As a result, MD can access larger length and time scales over quantum simulations. The advantage of MD is that it can predict exact system behavior within computer precision with respect to the model, ie. the potential functions of the constituent parts. It can also be used to compute dynamic properties of a system such as time-dependent system responses, vibrational spectra, and transport coefficients [25]. Computing power still limits the upper bound of time and length scales realistically accessible by MD simulations, however, due to the fairly direct proportionality between computing time and either particle number (size) or simulation duration (time). That said, there are natural limitations that limit the viability of utilizing MD simulations of macroscale systems in which trillions of individual atoms would be tracked for trillions of simulation time steps. MD simulation timescale is dictated by timing of interatomic collisions so that a fundamental time step is of order 10^{-15} s. This places a natural limit on the time scale accessible realistically accessible by MD. Brownian Dynamics (BD) simulations resolve electron degrees of freedom and therefore their timescale is governed by the collisions between tracer particles tracked through a solvent, which itself is not explicitly modeled. Hydrodynamics (HD) rely on aggregate thermodynamic properties such as density and viscosity; therefore, they average over significant degrees of freedom but, in doing so, are able to address physical behavior over very long relative time and length scales.

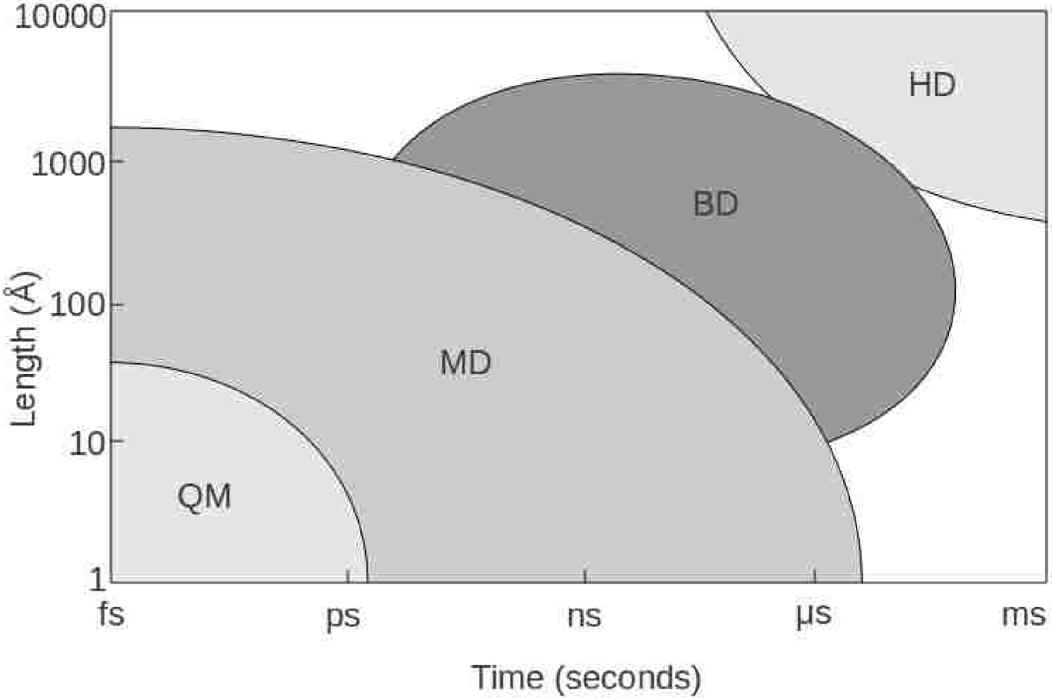

Figure 2.2 Approximate time and length scales accessible via different modeling techniques; quantum mechanics (QM), molecular dynamics (MD), Brownian dynamics (BD), and hydrodynamics (HD) [24].

It may be observed from the somewhat qualitative depiction of the scope of respective simulation techniques in Figure 2.2 that there is decided overlap of the scales attainable with the four major numerical techniques. Brownian dynamics and hydrodynamics, in particular, are competing methods for the study of wetting behavior. It is thus important to demonstrate the basic principles and assumptions on which those techniques are built so as to gain a better understanding of the advantages, and subsequently the limitations, of simulation methods germane to thermal spray modeling.

Brownian dynamics is useful in simulating the behavior of a system comprised of components with widely separated time scales, where one form of motion within the system is much faster than another. Thermal molecular vibrations, for example, are reproduced in MD at the femtosecond scale, while the bulk motion of nanometer scale liquid drops occurs at timescales on the order of hundreds of picoseconds, making MD or MC simulations of such behavior computationally intensive (though not prohibitively so). Brownian dynamics present a way around this hurdle by simplifying the equations of motion and removing rapidly varying degrees of freedom. The classical Langevin equation

$$\dot{p}_{i\alpha} = -\xi\, p_{i\alpha}(t) + \mathring{p}_{i\alpha}(t) \tag{12}$$

describes Brownian motion, which is expected for a particle being impacted randomly and rapidly by neighboring particles in a liquid. At short time, the dynamics of this motion is not physical, but for longer times particle displacements as described by Equation (12) conform to Einstein's relation

$$2\,t\,D = \frac{1}{3}\langle|\boldsymbol{r}_i(t) - \boldsymbol{r}_i(0)|^2\rangle \tag{13}$$

with ξ related to the diffusion coefficient D as

$$\xi = k_B T / mD \tag{14}$$

Thus Brownian dynamics presents itself as a particle-based technique where the solvent in which the particles are modeled is implicitly represented [23].The relatively coarse-grained nature of the technique also means that it is not useful in the analysis of system data at very fine temporal resolutions, as short-term physics are not represented accurately. For these reasons, the study of rapidly evolving high temperature capillary behavior is one to which Brownian dynamics is particularly poorly suited.

Hydrodynamic descriptions of wetting behavior are derived from classical fluid mechanics. At their heart, hydrodynamic models describe the dynamics of a fluid system through the interaction of a number of macroscale (continuum) thermodynamic quantities. The Navier-Stokes equations are a continuum representation of fluid motion, and are written in their most general form as

$$\rho\left(\frac{\partial \boldsymbol{v}}{\partial t}+\boldsymbol{v}\cdot\nabla\boldsymbol{v}\right)=-\nabla p+\nabla\cdot\underline{T}+G \qquad (15)$$

where ρ is density, p pressure, $\underline{\boldsymbol{T}}$ the stress tensor, and G all external body forces acting on a fluid element of differential volume. If the fluid is assumed to be incompressible, as is typically done for liquids, the equations become

$$\rho\left(\frac{\partial \boldsymbol{v}}{\partial t}+\boldsymbol{v}\cdot\nabla\boldsymbol{v}\right)=-\nabla p+\mu\nabla^2\boldsymbol{v}+G \quad . \qquad (16)$$

It is important to emphasize that the differential element considered in continuum dynamics is not the same as the particle discussed in MC, MD, or Brownian dynamics. Indeed, in a continuum scale model, quantities such as density and viscosity are derived from the macroscale averaged effects of the behavior of all the constituent atoms within a fluid volume increment, but individual atoms are not resolved. Each entity—or particle—in a MD simulation is an atom or molecule. Note that density and viscosity can not be defined for individual atoms in the same way that, say, velocity or energy can. Thus it is fundamentally incorrect to apply the Navier-Stokes equation of fluid motion to atomic particles; the input parameters necessary in describing a fluid via Navier-Stokes require a pre-existing knowledge of certain physical properties—viscosity, density, temperature—of the system because they are not determined inherently through the solution to the equations. Furthermore, the Navier-Stokes equations can not be solved analytically for most flow regimes, meaning that to apply them to the study of wetting phenomena, concessions must be made to adapt them by way of approximation.

Hydrodynamic theories of wetting behavior, then, can be seen to have a distinct limit in terms of their capability in describing fluid behavior at very small time and length scales. Additional challenges are placed where solid boundaries themselves interact with the fluid, or in wetting behavior where phase changes occur. Because the N-S equations describe only fluid motion and not particle interaction, such effects can not be captured in hydrodynamic wetting theory unless additional terms or functions are applied to correct for unaccounted physical behavior. So, while fluid dynamics has traditionally been studied via continuum simulations, or perhaps Brownian dynamics simulations, motivation exists to bring more fundamental length and time scale descriptions to bear. In other words, it is of interest to resolve degrees of freedom that both BD and continuum scale models average over in order to better reveal fundamental fluid mechanics mechanisms. This can provide greater detail on how reactivity, phase transformation, heat flow, and wetting couple during a highly non-equilibrium process. It is hoped that such knowledge can benefit understanding of non-equilibrium thermomechanical phenomena in general. As such, more recent research in wetting has applied atomic scale, molecular dynamics and Monte Carlo techniques.

2.2 Atomic scale numerical simulation techniques

As mentioned previously, simulations at the atomistic scale can provide useful physical insights. The proper resolution for atomic systems can not viably be obtained through BD or continuum models. Quantum mechanical scale descriptions, while atomistic, are very computationally intensive because electronic degrees of freedom are resolved. As such, one can not model a physical system of sufficient size to address questions related to drop impact. Two general methods for simulating many-body systems at the atomic scale are classical Monte Carlo (MC) and molecular dynamics (MD) methods. They represent two traditional classes of simulations, with MC covering stochastic and MD covering deterministic simulation trajectories. Such simulations do not explicitly account for electronic degrees of freedom. Therefore, they forego the mathematical complexity of solving the Schroedinger equation for the particle ensemble [24].

Electronic degrees of freedom, and therefore chemical identity, are represented implicitly in the description of the interaction potential energy between atoms. Modeling chemical interactions will be discussed further in subsequent sections, but the general approach is to employ some mathematic dependence of the interaction potential energy between two atoms on the atomic configuration of those atoms. As such, electronic degrees of freedom are coarse grained—or averaged-over—and subtleties of atomic interaction manifest in the atom-specific potential energy functions. With an interaction potential energy function, one can compute the energy of an atomic ensemble. Because the force on an atom is the negative of the spatial derivative of the atom's potential energy, this also provides a mathematical means to compute atomic scale forces as a function of the ensemble.

2.2.1 Monte Carlo method

Monte Carlo simulations essentially work as an algorithm to find the lowest free energy of a particle ensemble. By probing every degree of freedom for each particle through trial moves, MC simulations track the energy change of a system of particles (ie. atoms or molecules). Trial moves may include, for example, atomic displacements, position swaps between two atoms, or system volume changes. A given trial move is accepted if it lowers the system energy. If the trial move raises the system energy, the move is accepted with probability given by a Boltzmann statistical probability distribution:

$$\frac{N_i}{N} = \frac{g_i e^{\frac{-E_i}{k_B T}}}{Z(T)} \quad . \tag{17}$$

N_i / N is the fraction of particles at state i with energy E_i out of the total number of a particles, g_i is the degeneracy of the energy state, k_B is the Boltzmann constant, and T is the temperature. $Z(T)$ is the partition function,

$$Z(T) = \sum_i g_i e^{\frac{-E_I}{k_B T}} \quad . \tag{18}$$

This indicates a probability that an ensemble will occupy a given energy state. Thus, if a trial move raises the system energy, the Boltzmann distribution gives a quantitative likelihood that the move should be accepted. If a random number is selected that satisfies the computed probability, the simulation accepts the ensemble change. If not, the ensemble is restored to the pre-trial move state and the simulation continues with a new trial and move [23]. This technique is particularly useful in simulating equilibrium behavior in a system. It is not suitable for probing system dynamics of central interest to understanding fundamental flow mechanisms in reactive high-temperature capillary systems.

2.2.2 Molecular dynamics method

Though molecular dynamics is a tool that has come alive in the past few decades due to the evolution of truly widespread, high-powered computing, its history extends further back. B. J. Alder and T. E. Wainright conducted simulations of phase transition in the late 1950s. This early work used a system comprised of hard spheres colliding in a manner akin to billiard balls. A. Rahman simulated atomic interaction through the use of a continuous Lennard-Jones interatomic potential energy function in 1964. This simulation is notable for being the first to integrate the equations of motion with a finite difference method, which Alder and Wainright did not employ in their earlier study [24].

The unique aspect of MD simulations which can be gleaned from this comparison of techniques is that it does not actually have a theoretical upper boundary on the length or time scales which it is capable of simulating. Therefore the size of the system under examination and the length of the simulation is limited by the computing capacity (and patience) available to the researcher. This makes MD an effective tool in narrowing the gap between microscale and macroscale theories of physical phenomena [25]. Continued gains in computing power promise to expand the size and scope of MD simulations. That said, it must be acknowledged that practicality still limits the applicable size and time scale for MD simulations. Extending significantly beyond hundreds of nanometers and hundreds of nanoseconds is prohibitive. To enable state of the art scale MD calculations, a number of programs for parallel computing have been developed and released, such as LAMMPS, which is an open source code that is used herein [26].

Molecular dynamics simulations assume atomic ensembles can be represented as a group of interacting, point-wise massive particles. Through point-wise particles, classical MD atoms interact with one another in a manner which suppresses the very close approach of neighboring atoms; thus, atoms have an effective size. More will be said on this below. MD methods use a finite difference method to track atomic trajectories discretely in time. Simulation behavior is dictated by the system's Hamiltonian, and the integration of Hamilton's equations of motion results in the advancement of atomic position and calculation of velocity at those respective positions. As with MC simulations, MD simulations require the definition of a model of particle interactions, or an atomic interaction potential energy function. For brevity this model is called the potential function, and is constructed to reproduce experimentally observed behavior as well as obey fundamental laws such as energy conservation. It governs the interaction between system particles—typically atoms or molecules. Unlike MC, MD requires atomic or molecular scale forces in addition to energies. These two are intrinsically linked, however; atomic forces are obtained as spatial derivatives of atomic potential energy. Thus it can be seen that the potential function used in MC or MD simulations is solely determinant of simulation results, for a given thermodynamic ensemble.

2.2.3 Derivation of classical molecular dynamics model

Classical MD treats atoms as point-wise particles with mass determined by chemical identity. It is worth noting that while some MD models treat entire molecules as individual particles(ie. a form of atomic coarse graining), herein all such “particles” in a MD simulation are referred to as atoms. Atoms, then, interact with one another according to an interatomic potential energy function. For such a system of interacting, nuclear masses where electron motion is not explicitly resolved, system dynamics are well described via a Hamiltonian formulation. A system's Hamiltonian H is comprised of an internal and external part, such that

$$H = H_0 + H_1 \tag{19}$$

where H_0 is the internal component, given as the sum of kinetic and potential energy components

$$H_0 = KE + PE \quad . \tag{20}$$

Kinetic energy *KE* has the form

$$KE=\sum_{i=j}^{N}\sum_{\alpha}\frac{\boldsymbol{p}_{i\alpha}^{2}}{2m_i} \tag{21}$$

and potential energy *PE* is expressed in terms of interactions between atom pairs, atom triplets, quadruplets and so on as

$$PE=\sum_{i}^{N}u_1(\boldsymbol{r}_i)+\sum_{i}\sum_{i<j}u_2(\boldsymbol{r}_i,\boldsymbol{r}_j)+\sum_{i}\sum_{i<j}\sum_{i<j<k}u_3(\boldsymbol{r}_i,\boldsymbol{r}_j,\boldsymbol{r}_k)$$
$$+\sum_{i}\sum_{i<j}\sum_{i<j<k}\sum_{i<j<k<l}u_4(\boldsymbol{r}_i,\boldsymbol{r}_j,\boldsymbol{r}_k,\boldsymbol{r}_l)+\ldots \tag{22}$$

where α represents each of the different coordinates (x, y, z) and *m* is the mass of each atom *i*; note there may also be a single atom energy, $u_1(\boldsymbol{r}_i)$, to represent external field effects. Further subscripts *i*, *j*, *k*, and *l* refer to individual atoms and the summations run through all of the possible interactions between them, ***p*** and *m* are the atomic momentum and mass, respectively, ***r*** is the atomic coordinate vector, and u_n represents atomic contributions to the interaction potential due to groups of *N* atoms. The external component of the Hamiltonian, H_1, includes system uniform time dependent effects and external fields [2]. It can be seen by Equation (23) that the system's energy, or Hamiltonian, is conserved:

$$\frac{\partial H}{\partial t}=0 \tag{23}$$

These expressions conform to Newton's equations of motion, but obtain the description of particle trajectories based on their current state properties—namely kinetic and potential energy [5,23].

2.2.4 Particle interactions

Fundamental to any atomic scale simulations is the model used to describe interactions between constituent atoms. As seen in Equation (22), an interaction model can be decomposed into separate terms associated with increasingly larger clusters of atoms. A pair interaction (u_2) may, for example, represent a bonded interaction between adjacent, or neighboring, atoms. A three-body potential term (u_3) is typically used to constrain bond angles via bond-bond interactions. In that case, for atoms i, j, and k, the bond between i and j interacts with the bond between i and k. In addition to this, interaction models are also typically divided into terms contributing at relatively short range distances and terms contributing at relatively long range distances. The short range may span on the order of a few multiples of the nearest atom separation distance. Long range interactions may, in principle, span to an arbitrarily long distance. For many chemical systems, a robust approximation is to disregard long range interactions. The reasoning behind this comes about as a result of the vast domination of short range forces over long range ones at this small scale. Practically speaking, for short range models, atomic clusters only need to be considered out to the distance beyond which interactions are assumed to be so negligible as to go to zero. This distance is known as the cutoff radius.

For many material systems, it is possible to accurately describe their properties using interaction models that neglect terms for clusters of three atoms and larger. That is, some interaction models use only pair wise potentials. Such interaction potentials are then utilized in a summation of the system total potential energy, U

$$U=\sum_{i<j}^{N} u(r_{ij}|r_{ij}<R_c)+U_{lrc} \tag{24}$$

where r_{ij} and R_c are the separation distance between i and j and cutoff distance, respectively. The form of $u(r_{ij})$ is typically dictated by the type of interaction being modeled. For instance, different functional forms would be used to model Coulombic versus covalent interaction systems. Parameters in a given potential function are then dependent upon the specific atomic pair being modeled. For example, NaCl and KCl may both be described via ionic pair potential functions but parameters used in the function would differ. A long range correction factor, U_{lrc}, adjusts for those interactions neglected beyond the cutoff radius. It can be written as

$$U_{lrc}=2\pi N\rho_0\int_{R_c}^{\infty} dr\, r^2 g(r)u(r) \tag{25}$$

with ρ_0 being the density of particles in the system and $g(r) = \rho(r) / \rho_0$ the radial distribution function. In practice, calculation of U_{lrc} may be neglected, again under the assumption that interaction energy—and resultant atomic forces—are dominated by short range interactions. This assumption may be justified by the many accurate predictions of material thermomechanical behavior made under the assumption of short range interactions. However, a more physically satisfying justification for the assumption of short range interactions can be found in quantum mechanics (QM) calculations. These have shown that the approximation of short range interaction dominance closely replicates screening of interactions contributed by particles beyond the cutoff distance (ie. those that are more than a few neighbors away) by interference of more closely-neighboring nuclei [25].

Because atoms are modeled as individual points without inherent volume in the simulation space, the potential function *u* must feature a strong repulsive regime for very short separation distances. For example, Coulombic interaction alone for an ionic system would permit atoms with opposite charge to approach zero separation distance with divergent interaction, or bonding, energy. As such, it is necessary to include a second, repulsive term in the interaction between oppositely charged ions to model nuclear core repulsion. Approximating a particle as a hard sphere alleviates this divergent behavior; atoms only interact when their radii overlap, at which point the resulting collision is purely elastic. A slightly more realistic approach has been to model repulsion between particles as if they are soft spheres, where atoms interact in a purely repulsive manner but their collisions are not purely elastic. Such approximations have provided some insight into certain atomic systems and formed the basis for a few early MD simulations [25]. However, depending on atomic species in a pair, there may exist a distance range over which attractive interactions dominate (ie. for oppositely charged ions). Even for non-ionic systems, chemical interactions between an atomic pair may manifest attraction over some range and repulsion for very close range. Interatomic potential energy functions—

or simply potentials—must be able to accurately represent details of the interaction for a given chemical system.

A well known example of an atomic interaction model based only on pair interactions is the Lennard Jones model. This model assumes only weak, physical bonding mechanisms between atomic pairs (ie. dispersive, or induced dipole, forces). Repulsion at small separation distances is assumed to result from valence electron cloud overlap. The resulting potential is expressed as

$$u_{\alpha\beta}^{LJ}(r_{ij})=4\varepsilon_{\alpha\beta}\left(\left(\frac{\sigma_{\alpha\beta}}{r_{ij}}\right)^{12}-\left(\frac{\sigma_{\alpha\beta}}{r_{ij}}\right)^{6}\right) \tag{26}$$

The subscripts α and β denote the species of the particles. The Lennard-Jones potential function Equation (26) uses ε and σ to represent parameters dependent in the same way on α and β. For that potential, ε is the minimum potential energy and σ is the diameter of the particle. Additional interactions such as chemical bonding and Coulombic effects can be represented in the potential function similarly via a functional form that reflects their influence on system particles [23-25].

It should be kept in mind that many other potentials exist to represent the behavior of different particle ensembles. Namely, the embedded atom method (EAM) generates pair functionals for metal and metal alloy particles, which is useful in thermal spray simulations.

2.2.5 The EAM potential function

It is the goal of this research to use atomistic simulations to study metallic material properties. Pair potentials have been discussed above, but they can not properly describe the elastic properties of metal solids due to their failure to properly predict the Cauchy discrepancy observed in experiments. Specifically, pair potentials always give models of solids where C11 = C44; for metals, then, pair potentials can not replicate C11 ≠ C44, observed experimentally. The embedded atom method was developed during the early 1980s, explained briefly in a letter in 1983, and presented rigorously in a paper in 1984 by Daw and Baskes. It is an outgrowth of quasiatom theory and it was developed in response to the failure of pair potentials to accurately model metallic material properties [27,28].

A simplistic but still useful way to describe bonding in metallic systems is the "sea of electrons" approximation, in which the nucleus of each metal atom is considered to exist in—or be stabilized by binding with—a sea of electron charge created by all other atoms in the metal. A more robust description is that valence, or bonding, electrons are delocalized in a metal system, particularly when compared to covalent and ionic systems. The embedded atom method (EAM) was developed to model this type of bonding without explicitly invoking electron degrees of freedom, as is done in QM level theory. That is, the EAM was developed to enable accurate classical atomistic simulations of metal systems. The basis for the embedded atom method is the treatment of each atom in a solid as an impurity in a host lattice comprised of all the atoms in the rest of that solid. This leads to a relationship between the energy of the impurity as a function of the energy of the host sans impurities. Stott and Zaremba first represented the energy of the host solid as a function of impurity type and position,

$$E = f_{Z,R}(\rho_h(R)) \tag{27}$$

where Z and R are impurity type and position, and ρ_h is the “unperturbed” host electron density. The function f is some universal function of unknown form, independent of host atom type; it can be thought of as giving the energy to embed impurity Z into electron density $\rho_h(R)$ at position R in the host. Treating each atom in the solid as an impurity, then, allows for the quasiatom concept to be applied to the total energy of a system of N atoms as

$$E_{tot} = \sum_i F_i(\rho_{h,i}) \tag{28}$$

with F_i being the embedding energy and $\rho_{h,i}$ the host electron density at the position of atom R_i, where atom i itself is not included. The embedding energy of an atom, then, is defined as that of the atom in a uniform electron gas relative to the atom separated from the electron gas. It should be noted here that the embedding energy F is not assumed to be trivially related to the universal function f.

To account for nuclear repulsion at small separation distances, the total energy can be modified into the definitive expression

$$E_{tot} = \sum_i F_i(\rho_{h,i}) + \frac{1}{2}\sum_{i \neq j} \phi_{ij}(R_{ij}) \tag{29}$$

The first term is the energy contribution expression of Equation (28); in the second term ϕ_{ij}, is a short range pair potential that is a function of R_{ij}, the distance between atoms i

and j. The form of ϕ_{ij} depends on the type of atom pair. The host electron density is

$$\rho_{h,i}=\sum_{i\neq j}\rho_j(R_{ij}) \quad , \tag{30}$$

and it can be seen, then, that embedded atom model employs pair functionals. Equation (29) can thus be used to calculate the properties of atoms in a solid, such as lattice constant and sublimation energy. As is done with most classical interaction models, EAM potentials are typically forced to go to zero at some cut-off distance. For EAM potentials, this distance is typically chosen so that, for a ground state (face-centered cubic) crystal, interactions are included out to either the second or third neighboring atomic shells. The justification for EAM functions F_i, ϕ_{ij}, and $\rho_{h,i}(R_{ij})$ can be determined based on comparison with experimental data of an element's or alloy's physical properties. As a result of this derivation, and empirically-derived functions based on verifiable material thermomechanical properties, the EAM potential model has been shown to accurately represent the behavior of metals and their alloys [27,28].

Work presented here will explore behavior for aluminum (Al) and copper (Cu) binary metal systems. The EAM potential functions, or interaction model, for this system are taken from literature [29,30]. This set of interaction functions has been shown to accurately reproduce the mechanical behavior of pure Al, Cu, and alloys of the two. Figure 2.3 is a plot of interatomic energy versus lattice constant for Al derived via the embedded atom method. A similar plot (not shown) can be created for Cu.

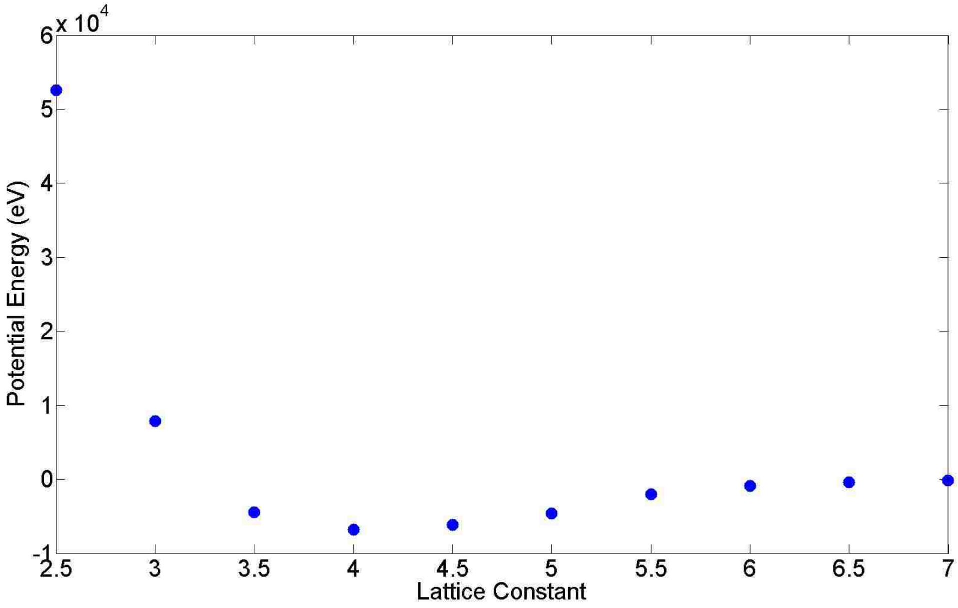

Figure 2.3 Plot of potential energy as a function of lattice spacing for Al, generated from EAM potential function in LAMMPS.

2.2.6 Integrators

As stated earlier, the MD simulations also require an integrator to compute particle trajectories. This integrator is the driver of the simulation and its implementation directly controls its accuracy. The accuracy of the simulation results depend on the fidelity of the integrator, and it must be remembered that no finite difference method can generate precisely perfect results with zero error. The integrator's accuracy in approximating true particle trajectories is critical, and can be checked against analytical solutions to simple systems. It must also be a stable and robust algorithm able to conserve energy, handle disturbances, and allow for sufficiently large time steps to move the simulation forward efficiently in time. A number of integrators exist, from the simplest based on a Taylor series expansion, to operator splitting methods. The Verlet-

Störmer integrator (commonly referred to as the Verlet algorithm) is based on a Taylor series expansion of particle position. It is, nonetheless, likely the most widely used method of integrating the equations of motion presented henceforth. From *t* to an appropriately small time step *δt*, the position ***r*** is written as

$$\boldsymbol{r}(t+\delta t)=\boldsymbol{r}(t)+\boldsymbol{v}(t)\delta t+\frac{1}{2}\boldsymbol{a}(t)\delta t^2+\frac{1}{6}\boldsymbol{b}(t)\delta t^3+... \tag{31a}$$

and the velocity as

$$\boldsymbol{v}(t+\delta t)=\boldsymbol{v}(t)+\boldsymbol{a}(t)\delta t+\frac{1}{2}\boldsymbol{b}(t)\delta t^2+\frac{1}{6}\boldsymbol{c}(t)\delta t^3+... \tag{31b}$$

The second, third, and fourth time derivatives of position are ***a***, ***b***, and ***c***. The same approximation can be made for the backwards step -*δt* and added to the first set of expressions to yield new position and velocity:

$$\boldsymbol{r}(t+\delta t)=2\boldsymbol{r}(t)-\boldsymbol{r}(t-\delta t)+\boldsymbol{a}(t)\delta t^2+O(\delta t^4) \tag{32a}$$

$$\boldsymbol{v}(t+\delta t)=2\boldsymbol{v}(t)-\boldsymbol{v}(t-\delta t)+\boldsymbol{b}(t)\delta t^2+O(\delta t^4) \tag{32b}$$

The accuracy of Taylor expansion-type integrators is not the greatest among all types of integrators, but serves as a very straightforward demonstrative example of the mathematics powering an MD simulation [23].

2.2.7 The velocity Verlet algorithm

The standard Verlet integrator is a very compact and easily-programmed one, and is completely time-reversible and demonstrates excellent energy-conserving properties over a range of algorithm time step sizes. Modifications of the original Verlet algorithm have been made to improve upon it, however, and the so-called leap-frog and velocity Verlet algorithms have been presented to better handle particle velocity information and alleviate numerical imprecisions which arise from using the original Verlet. The leap-frog method will not be discussed here, and the reader is directed towards Reference 5 for further information.

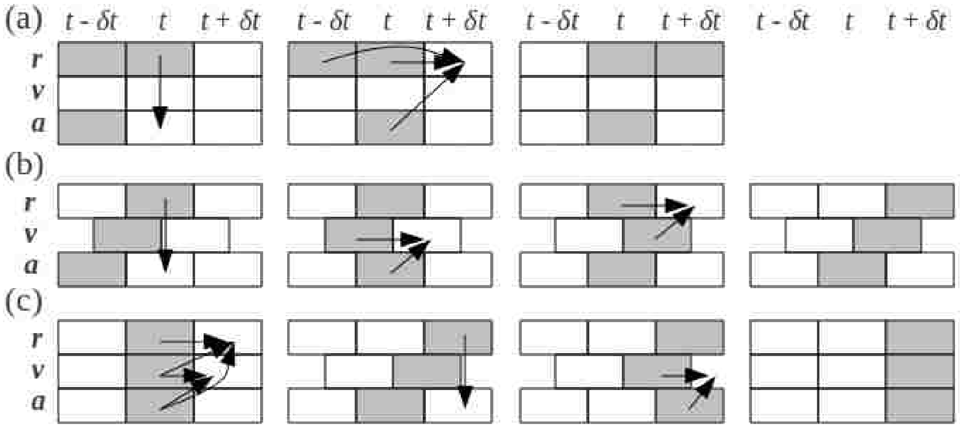

Figure 2.4 Different forms of the Verlet algorithm; (a) is the original Verlet method, (b) is the leap-frog variation, and (c) is the velocity Verlet form. Successive steps for each algorithm are shown. Note the shaded boxes represent stored variables [23].

The velocity Verlet algorithm stores particle position, velocity, and acceleration at time *t* while minimizing round-off error. It is expressed as

$$\boldsymbol{r}(t+\delta t)=\boldsymbol{r}(t)+\delta t\,\boldsymbol{v}(t)+\frac{1}{2}\delta t^{2}\boldsymbol{a}(t) \tag{33a}$$

$$\boldsymbol{v}(t+\delta t)=\boldsymbol{v}(t)+\frac{1}{2}\delta t\,[\boldsymbol{a}(t)+\boldsymbol{a}(t+\delta t)] \tag{33b}$$

It is similar to a three-value predictor-corrector algorithm were the position corrector coefficient in the latter is equal to zero. It involves two computations per time step separated by a force evaluation term. First, new particle positions are computed via Equation (33a) for time $t + \delta t$. Velocities are computed at the mid-step time $t + 1/2\delta t$ via the equation

$$\boldsymbol{v}(t+\frac{1}{2}\delta t)=\boldsymbol{v}(t)+\frac{1}{2}\delta t\,\boldsymbol{a}(t) \tag{34}$$

At this point, forces, potential energy, and accelerations are computed for the next time step $t + \delta t$. Then the final velocity for the step at time $t + \delta t$ is calculated as

$$\boldsymbol{v}(t+\delta t)=\boldsymbol{v}(t+\frac{1}{2}\delta t)+\frac{1}{2}\delta t\,\boldsymbol{a}(t+\delta t) \tag{35}$$

and the kinetic energy for the particles can then also be computed. The memory footprint of this method is modestly greater than the unmodified Verlet algorithm, and the numerical stability and simplicity of this algorithm make it a very attractive improvement upon the original Verlet integration method [23]; it is also the algorithm on which LAMMPS MD simulations run.

2.2.8 The atomic ensemble

The goal of the formation of the algorithms and models presented above is to ultimately form a tool which can use atomic simulations to perform statistical thermodynamic calculations for a given system. To do this, as is the case in many calculations, certain thermodynamic properties must be specified and remain constant for the duration of the calculation while others are kept as variables. The control of these thermodynamic parameters characterizes the thermodynamic ensemble. The microcanonical ensemble (NVE) can be thought of as the natural ensemble for a MD simulation. Without time dependent external force interactions the system's Hamiltonian will remain constant and system dynamics will evolve on a constant energy surface. The canonical ensemble (NVT) is the simplest extension of the microcanonical NVE, and quantities of temperature T, number of particles N, and volume V are controlled by certain controller algorithms. These algorithms operate on system quantities in one of a variety of ways: differential, proportional, integral, and stochastic.

A differential controller fixes a thermodynamic quantity at a prescribed value and does not allow the ensemble's average to deviate from this prescribed quantity. Proportional control corrects the value of thermodynamic properties through a coupling constant towards a prescribed value; this constant dictates the strength of fluctuation about the prescribed property value. Integral control represents the effect of an external system which fixes the ensemble state. The evolution of thermodynamic properties is driven by the equations of motion derived from the system's Hamiltonian. Finally, stochastic control propagates thermodynamic properties via modified equations of motion in which certain degrees of freedom are modified stochastically to generate the desired average thermodynamic property values [23,24].

The above are four types of control mechanisms which can be implemented into the MD algorithm to control temperature or pressure—ie. to act as thermostats or barostats—which serve to fix thermodynamic ensembles. Temperature and pressure can be represented in an MD simulation as

$$T=\frac{2}{3}\frac{KE}{N\,k_B} \tag{36}$$

$$p=\frac{N\,k_B T}{V}+\frac{\sum_{i}^{N}\boldsymbol{r}_i\cdot\boldsymbol{f}_i}{dV} \quad . \tag{37}$$

By altering the velocity *v* or the volume *V* of the particles or simulation box, respectively, the algorithm can control the temperature, pressure, and all coupled thermodynamic quantities associated with them [26]. The Nosé-Hoover controller is a an example of a differential thermostat/barostat; it is widely implemented in MD algorithms—it is used by LAMMPS, for instance—because it maintains the ergodic ensemble. By maintaining ergodicity, it ensures that a simulation samples the entirety of the thermodynamic space [23-25].

3. Development of Thermal Spray Model

3.1 LAMMPS software package

This work utilizes a preexisting molecular dynamics (MD) package called LAMMPS. LAMMPS is distributed by Sandia National Laboratories, available free of charge for download over the Internet. The name is an acronym for Large-scale Atomic/Molecular Massively Parallel Simulator. It is an open-source, massively parallel classical MD code capable of modeling a wide variety of materials in solid, liquid, or gaseous state. The standard download includes a library of potential functions and is capable of reading from any other properly formatted potential function files that might be imported by the user. For simulations of metals and metal alloys, however, the included embedded atom method (EAM) potential is a proven model of ground-state properties for metals [26-29].

3.2 The simulation system

Having introduced the EAM potential functions governing the behavior of the two model metals to be used in the simulation, it is important to understand the metallic system and initial conditions developed for use in our simulations. The overarching goal is to develop MD models of molten metal droplet impact onto solid metal surfaces. To connect our simulation results with existing experimental data, the Al-Cu system is selected. In this research, the drop is copper liquid Cu(*l*) and the substrate is a single face-centered cubic (FCC) crystal of aluminum Al(001). Thus, this work requires preparation of a multi-phase system with highly non-uniform temperature distributions. Furthermore, the model must properly represent complex impact physics when the drop impinges on the surface. Steps taken to achieve this model—and verification of its performance—are presented in this chapter.

3.2.1 Determination of equilibrium lattice constant

The process of drop impact on a solid surface is considered as a form of dynamic wetting, or capillary flow, phenomena. As a precursor to any dynamic wetting simulation, both fluid drop and solid substrate must be equilibrated. In a simulation environment, as in an experimental setting, this requires a number of steps to be taken to ensure the integrity of the forthcoming results. Thermal expansion, as with the rest of the mechanical properties, of Al and Cu in the model used here is in close agreement with experiments [31]. Nonetheless, it was necessary to determine the model's quantitative relationship between density (ie. lattice constant) and temperature. Thus, the equilibrium lattice spacings for EAM copper and aluminum at specified temperatures were determined through simulations of respective metal crystals.

A small cubic model Al crystal was first simulated at NPT conditions for sufficient time for the crystal to relax to an equilibrium volume for the imposed temperature T = 300 K. By creating a small cubic metal crystal (8 x 8 x 8 unit cells) based on published lattice spacing data at temperature T = 0 K [31], the resulting volume —and other thermodynamic quantities, for that matter—can be output directly from a LAMMPS simulation, and this data monitored in real time with simulation progress to provide information on system behavior. Periodic boundary conditions ensured that the number of atoms in the system could be kept small without surface effects skewing the behavior of the crystal; temperature was controlled by a Nose-Hoover thermostat (see Chapter 2). The block was thus allowed to relax to an equilibrium volume, and that volume was used to directly calculate lattice constant for the cube, a. Volume for a cube was thus fixed based on the NPT simulation result, and a number of NVT simulations were launched with slightly (~ 0.0005 Å) varied lattice spacings. Pressure was monitored, and corrections made to the lattice constant such that varied iterations of the cube dimensions yielded a lattice constant which held at constant volume and nearly zero absolute pressure. In this way, an unstressed perfect crystal lattice constant was deduced. It was found that the EAM potential model for pure aluminum at this temperature yielded an equilibrium lattice constant of a_{EQ} = 4.0856 Å.

Based on this, a larger crystal was able to be created and equilibrated at the same conditions in a relatively short-duration simulation. The dimensions of the model substrate for impact simulations are discussed below. However, it should be noted that, in order to create a substrate from a three-dimensional periodic or “bulk” crystal, periodic boundary conditions must be removed in one dimension. This was applied in the z direction so that, for a FCC crystal, a (001) surface formed at both upper and lower ends of the system in z. A subsequent simulation in a NVT ensemble allowed for surface relaxation, or equilibration as termed here. Note that the usage of the term NVT in this description is not strictly correct; the crystal was unconstrained against expansion or contraction in the free surface (z) direction. Such relaxation phenomena are typically localized to the two or three atomic planes nearest to the free surfaces. Because the simulation cell sizes in x and y, L_x and L_y, are fixed, this means atoms atoms more than three atomic planes away from the free surfaces in z are in a zero stress state (ie. $p = 0$ in the majority of the crystal). Also note that, following surface relaxation, atoms within roughly z = 2.0 nm of the lower free surface are held frozen in space for all subsequent simulations. This is intended to model a transition to an infinite crystal in negative z space. It is common practice in MD simulations, as it is in finite element analyses, for instance, to ground such a region rigidly in space to prevent translation of the entire body attached to the region upon application of an external force acting on the body.

3.2.2 Creation of constituent simulation bodies

As the copper potential was to be used to form the liquid metal drop, the establishment of its equilibrium lattice constant was not undertaken. Instead it was first necessary to equilibrate a Cu(*l*) bulk (ie. three-dimensional periodic) sample at the desired drop temperature. A target temperature value of $T = 1500$ K was obtained as a convenient state point roughly 10 % above published copper melting temperatures. It should be understood that the model used here predicts a melting point for pure Al and Cu to within 10 % of experimental values. Also note that the model predictions for melting point are both below their corresponding metal's experimental value. To obtain a Cu(*l*) drop at $T = 1500$ K, it was first necessary to equilibrate a rectangular Cu(*l*) block at $T = 1500$ K. To do this, it must be acknowledged that a barrier to melting exists for MD simulations of a perfect, three-dimensional periodic crystal. This thermodynamic anomaly results from the absence of any free surfaces or internal defects within the MD sample. In their absence, the liquid phase must nucleate in a bulk lattice. Such nucleation leads to an energy barrier, analogous to what happens when solidifying a melt. In the presence of crystallographic imperfections, liquid phase nucleation becomes barrierless and an experimental specimen will melt at the thermodynamic melting point. For a model, perfect crystal, as in these MD simulations, one can form a super-heated solid, with $T > T_M$, where T_M is the thermodynamic melting point predicted by the model. While equilibrium demands that the super-heated solid should melt, the barrier introduces a kinetic constraint. The size of MD simulation samples further aggravate this because the kinetics of phase transformation are abetted by long wavelength phonon contributions. The limited spatial extent used in a MD simulation places a physical cutoff on phonon wavelengths that can manifest. Thus, melting may be very difficult to observe in a typical MD simulation duration.

To overcome this kinetic constraint and thermomechanically induce liquid formation in the copper lattice, initial lattice spacing for the copper block was set approximately 35 % larger than solid copper has been reported to reach. Recall also that temperature in atomic simulations is given by the expression in Equation (36). An interesting manifestation of statistical mechanics, and specifically equilibrium particle theory, in MD simulations is that, when atoms in a perfect crystal lattice are assigned velocities to establish a given temperature for that lattice, this represents only the kinetic modes of energy within the system. Due to the description of the system's Hamiltonian in Chapter 2 (Equation (20)) comprised as the sum of kinetic and potential energy terms, equipartition theory demands that the energy in the system be evenly divided between kinetic and potential modes. In the preparation of our drop, velocities were assigned to correspond with a temperature T = 3000 K. The result of this was that the actual average temperature for the drop at $t > 0$ ps rapidly decreased and converged to T = 1500 K, thus saving computational time.

It is important to also understand the geometric constraints placed upon the system, and the reasons for the choosing of those conditions, in greater detail. Decisions were made based on a balance between computation time and geometric scale and complexity. Fully three-dimensional atomistic simulations were run in all cases; however, drop wetting was modeled in a pseudo-two-dimensional geometry. This was motivated out of considerations for computational speed; as established in Chapter 2, the length of time or “speed” of MD simulations is heavily dependent upon the number of particles comprising the model system, and so any means of minimizing the number of atoms involved in the simulation without decreasing its fidelity were employed. Based on a heuristic criterion for nm scale drops, the substrate surface dimension should be at least four times the diameter of the drop in the axis of spreading. Modeling a three-dimensional, spherical drop would require the surface width and depth to be increased to account for the two dimensions in which the drop would spread. Increasing the surface area by a factor of nearly 30 would thus increase the total volume by the same factor (assuming thickness is left unchanged) as well as the total number of particles comprising the Al substrate. In the same way that two-dimensional descriptions of other thermodynamic and fluid mechanic phenomena can greatly simplify the expressions describing them while being directly related mathematically to the three-dimensional case, it was decided that the two-dimensional model would permit the same fundamental flow and phase transformation physics to be elucidated at a lower computational expense. Our models, so established, are thus simulations of a infinite cylindrical drop, axial in y, impacting a substrate surface oriented in z. Because the simulations are periodic in x, this means we are modeling an infinite array of parallel cylindrical drops impacting a surface (though the model will be shown to be constructed such that drop-drop interactions will be negligible). Figure 3.1 depicts the system dimensions for reference.

The largest drop diameter D modeled was $D \approx 45$ nm; while this is a very small drop size for many thermal spray applications, there are some researchers now spraying nanometer scale particle size powders (see Chapter 1). Furthermore, we feel this represents a reasonable size range to be able to extract fundamental mechanisms of drop impact, wetting, and solidification while still hoping such mechanics, or their effects, can be scaled up to describe macroscopic drop behavior. This creates a balance between desired thermomechanical information and computational cost, and relevance to experimental particle size. Using the estimate that the substrate extent in the drop spreading direction, x, should be at least four times greater than the diameter of the drop [12], an Al substrate with dimension $L_x \approx 200$ nm was created in the manner outlined above. Substrate thickness was fixed at $L_z \approx 22.5$ nm; this value is further discussed below. Depth in y, L_y, though periodic and simulated to be infinite, was set to be $L_y \approx 7$ nm. This distance is roughly 15 times the range of the interaction model. These approximate, target dimensions for the substrate were transformed into precise dimensions by using the $p = 0$ (equilibrium) lattice constant for Al at $T = 300$ K. Equilibrated substrate dimensions as a result of this process were $L_x = 204.28$ nm, $L_y = 6.95$ nm, $L_z = 22.47$ nm.

The Cu(*l*) bulk equilibrated at $T = 1500$ K was forced to assume an identical dimension in y to the Al(001) substrate. This was constrained so that the atomic ensemble representing the Cu(*l*) drop could be eventually merged with the Al(001) substrate atomic ensemble while maintaining the $p = 0$, $T = 300$ K lattice constant for the substrate. The x and z dimensions of the Cu(*l*) slab were allowed to vary. Because the ensemble was liquid, this meant the NPT algorithm drove the system to zero pressure despite L_y being fixed. The L_x and L_z for the Cu(*l*) slab were chosen to be large enough to extract a drop of $D = 45$ nm (ie. $L_x \approx L_z \geq 45$ nm). After the Cu(*l*) block was equilibrated at $T = 1500$ K, a cylindrical drop with free surfaces in the x-z plane and periodic boundary conditions in y was extracted from the block. This drop was then run at NPT conditions, with fixed dimension in y and free surfaces in x and z to equilibrate it in free space.

It has been demonstrated in previous work [12] that the crystallographic orientation of the substrate lattice has negligible effect on the spreading dynamics of a drop such as the Cu one under consideration in this work. This is not a universal rule by any means, but for our metallic system and the mechanisms which it is designed to elucidate, it was assumed that any influence of crystal orientation on observed wetting dynamics would be negligible. The (001) orientation was thus chosen so as to yield a smooth atomic plane at the surface of z. It is understood that surface smoothness to within an atomic plane, as well as a precisely arranged monocrystalline structure are seemingly unrealistic, but it must be remembered that this work is not done to replicate perfectly a particular experiment or industrial process, but to provide insight into the mechanisms driving high temperature wetting. There is ongoing work investigating the role of surface conditions in wetting behavior [32-35], and the possibility remains for future MD simulations to be conducted with surface crystallography, topography or chemistry introduced as an independent variable. For the sake of this paper, again, such features are not investigated.

3.2.3 Simulation body preparation

A code manipulated the Cu(*l*) slab's ensemble data file to discard all atoms with positions in x and z beyond a given radius from the geometric center of the rectangular area, effectively cutting out a cylinder from the existing liquid Cu rectangle. For the program it is straightforward, but nonetheless necessary, to also re-assign atom identification numbers to the atoms within the system. A new data file must then be created. The specific tracking number, or “tag”, assigned to a given atom does not matter, but all tags must be in the range $1 \leq i \leq N$, where N is the total number of atoms present in the simulation space regardless of species (type). Position data for both Al and Cu drop were then combined into a single unified data file.

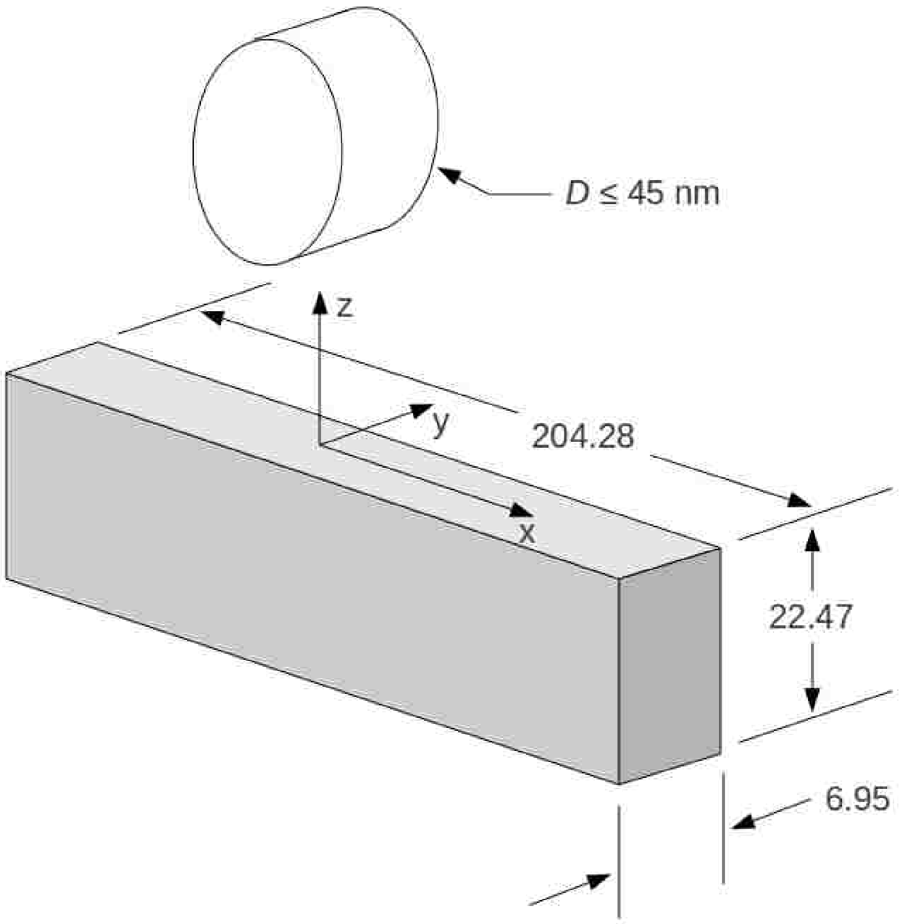

Figure 3.1 Dimensioned drawing of substrate and drop; ordinate axes are labeled and lengths are in nanometers. Drop and substrate size, separation, and proportions are not scaled.

With drop and substrate equilibrated separately, it was necessary to join the two atomic ensembles and establish the correct temperature and relative distances. The ensembles are saved from simulation run to simulation run via text files which include, among other information about the system, atomic positions in space. These coordinates were combined into a unified system data file and transposed via MATLAB program so that the drop and substrate were arranged as desired in the simulation space. To ensure the drop and substrate would not interact at initial simulation time $t = 0$ ps, the cutoff distance for the potential, R_c ~= 5.5 Å, was used as a guideline. The distance between the lowermost Cu atom in the drop and upper atomic plane of Al (at z = 0 nm) was set to 1 nm, or roughly twice the cutoff. This measure ensured a conservative initial gap between the drop and substrate while positioning the two bodies close enough such that, depending on velocity, impact would occur within the first few picoseconds of the simulation. The latter is an important consideration from the point of view of computation time. Note that all preparation and analysis programs developed in support of the research presented herein, as well as associated simulation input scripts and output data, will be preserved in a repository for future use by the research group.

3.2.4 Simulating infinite substrate depth

One final consideration must be taken into account before impact simulations are begun for a system of this physical size. Owing to the relative equivalence of drop diameter and substrate thickness, the contribution of pressure waves within the substrate can not be assumed to be negligible. In an experimental setting, these “shock waves” within the substrate are dissipated by means of damping of the bulk material itself. Dislocations in the lattice structure, surface roughness, and grain boundaries all provide means of diffusing a pressure wave that could form upon drop contact as a result of the sharp imparting of kinetic energy to the substrate. In addition to these sources of pressure wave diffusion, the sheer size of a test specimen substrate with the respect to a typical thermally sprayed drop is usually enough to ensure that a wave will not have sufficient time to travel through the substrate, reflect cleanly off of an opposing substrate surface, and return to the contact area in time to affect the dynamics of drop spreading. With respect to the size of the drop and the kinetic energy which its impact might impart to the substrate, then, it can be said that any industrial or experimental substrates act as infinitely large bodies. At a minimum, it must be acknowledged that impact waves are not expected to significantly influence the morphology of a solidified drop after impact and spreading upon a surface.

Such can not be said of the Al substrate simulated in this work. Most of the features of a real-world substrate which would normally prevent the propagation of a pressure wave are absent in a simulated substrate. There are no dislocations or grain boundaries in the substrate lattice structure. After equilibration, the crystallographic structure of the substrate is perfect. The surface, too, is perfect to the precision of an atomic plane of Al, so surface roughness is also completely neglected. Finally, and most importantly, the bottom ~ 1.3 nm of the substrate in z is rigidly fixed in space such that the thickness of the frozen layer was at least twice that of the cutoff distance, $L_{z,FROZEN} \geq 2R_C$. Though this is a necessary concession for the simulation to be properly constrained in absolute coordinates, it effectively creates a wall of infinite hardness off which a pressure wave could quite readily bounce.

As noted earlier, increasing the number of atoms in the simulation is an unappealing option. Additionally, to sufficiently attenuate a wave, the required extent in z would be enormous. Thus the most obvious method of creating greater substrate mass in the z direction to improve damping was not undertaken. A viscous damping region within the existing substrate is instead implemented so as to artificially simulate an experimental one without the need of imparting imperfections and surface topography. Indeed, the creation of a realistic surface within an MD simulation which is not truly massive in atomic scale still represents a huge undertaking. From a system dynamics point of view, the addition of a viscous damping layer is entirely justified, as it simulates natural attenuation of the spring-like nature of a metallic crystal by imperfections and bulk effects noted earlier.

Using the classic spring-mass-damper analogy, the impact can be thought of approximately as an impulse applied to the system at the time of contact of the drop at the surface. From here, the substrate can be assumed to respond in a second-order manner. It is thus desirable to create an over-damped response to the initial perturbation in the system. In this way, the system can absorb the impact through the upper regions close to the surface in an elastic way, as a real surface would locally deflect, but damp the oscillations induced in the stress distribution within the lattice structure of the substrate in a manner such that it does not reflect back to the atoms near the surface. Such reflecting waves are not only unrealistic for any real thermal spray scenario (or any real wetting scenario, for that matter) but are also dangerous in that their magnitude can be on the order of the forces driving drop wetting in the first place. The possibility of such distortion to the observed data makes the appropriate application of a viscous damping region a necessity for this simulation.

One caveat to the simple single damper model analogy is that all latices but the frozen region of atoms at the very bottom of the substrate have their own spring-like behavior, and there is an integrator present which itself can act to dampen reverberating pressure waves. Complicating the outlook is the understanding that thermal, kinetic, and potential energy all couple directly in an atomic, or MD simulation, ensemble. For instance, it is the collective mean vibration of atoms that represents the temperature, but not translational kinetic energy. Because a thermostatting integrator is necessary to maintain thermal energy in an atomic ensemble, it cannot be omitted and thus its coupling with the rest of the system must be considered. In the simulation system, then, as is often the case in the development of full-scale dynamic systems, a precise model of the response of the substrate is not pre-existing nor can it readily be determined. The most expedient method to determining a stable viscous damping region is thus taken to be an experimental one, albeit a computational experiment.

Assumptions were made regarding the demarcation of the different regions within the merged simulation system. Whereas it was appropriate in the equilibration of the solid and liquid subsystems to apply thermostatting to all atoms in the ensemble, this is discouraged in the wetting simulations for three reasons:

- Applying a thermostat controller to the drop would influence its wetting dynamics in an unphysical manner
- No position/velocity integrator should to act on the frozen or “grounded” atoms.
- Thermostatting the surface region with which the drop directly interacts would unnaturally influence the thermal (and thus kinetic) behavior of drop spreading. As the simulation is being used to yield insights into high temperature capillary spreading, this is unacceptable. However, heat should be removed from the

surface via conduction in the same manner as what would be observed in an experiment.

With this in mind, it was decided that the substrate would be divided into regions with varying definitions as shown in Figure 3.2. It should be remarked that lines of demarcation were placed such that a region demarcation would not fall within an atomic plane. The unconventional dimension for the frozen region is a result of choosing the first six atomic planes from the bottom of the substrate. This distance ensures that mobile atoms directly adjacent to the frozen region do not sense the presence of the free surface at the bottom (negative z) face of the substrate; the free surface is well beyond the cutoff distance of the atomic model.

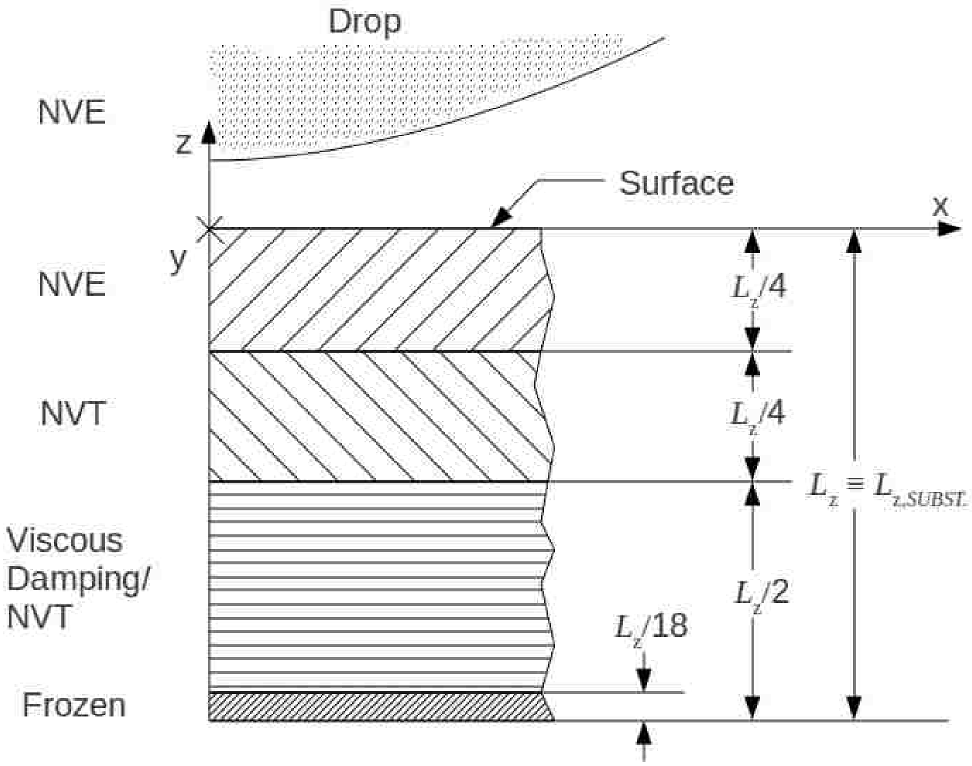

Figure 3.2 Schematic of regions within Al substrate. Note that NVE refers to constant volume and energy time integration and NVT to constant volume and temperature. Frozen and viscous damping are explained in text.

The relative sizes of the substrate regions were chosen based on three considerations:

- The viscous damping is to be sufficient to remove the influence of reflected waves on drop spreading and final particle morphology.
- The NVE region of the substrate must be sufficiently deep to prevent drop intrusion into the thermostatted (NVT) region of the substrate, which could skew the results of the simulation.
- The pure NVT region will have to act sufficiently as a buffer between the viscous damping region and the NVE region. Because electronic degrees of freedom are not included in the model potential function, the thermal conductivity of Cu and Al in the simulation can be as much as ten times lower than what is observed in these materials experimentally. Hence, heat must be removed aggressively from the system so that physical thermodynamic behavior can be approximated.

It was decided based on these criteria that the damping region would comprise roughly half of the substrate, with the remaining half being divided evenly between the NVE and NVT regions.

Damping is achieved by coupling a thermostat with a viscous damping boundary condition in the region comprising the bottom half of the substrate with the NVT and NVE comprising the upper half, as shown in Figure 3.2. In principle, the appropriate magnitude of γ should relate to physical properties. As stated before, here it is easiest to use computational experiments. The goal is to find a value $\gamma_{MAX.}$ such that normal NVT control can still maintain $T \approx 300$ K. It is required that $\frac{dT}{dt} = 0$ in the substrate before wetting simulations are conducted.

An array of simulations were begun with substrates divided as described above, each having a different value for the viscous damping region. The temperatures for each region were output and observed over time to determine the maximum damping which the system can withstand without dissipating its thermal energy in the viscous region or achieving a resonance in the integrators which could cause system instability. It was decided that the viscous region would also feature a spatially-progressive damping rate in the z direction (ie. damping coefficient γ would increase as a linear function of negative z) to maximize the absorbing capabilities of that region with respect to pressure waves. This ramped damping required the further division of the viscous region into the desired amount of cells—25 regions was the target used—so that a linearly-increasing damping rate could be simulated.

Simulations were run with a single γ value for all the damping regions initially to determine the maximum average damping for which $\frac{dT}{dt} = 0$ and $T \approx 300$ K. Plots of the temperature as a function of time are presented in Figure 3.3. Temperature is reported as a time-averaged quantity every 0.1 ps. For each data point, 100 instantaneous samples of 425018 atoms are used to compute the temperature. Successive plots show the results of progressive simulations, from an initial trial with $\gamma = 1.0$ to $\gamma = 0.000050$ eV-ps/Å^2. The final value of γ was observed to work in conjunction with the thermostat input to oscillate and converge about the target $T = 300$ K in an underdamped fashion; oscillations are permissible as further equilibration of the Al block allows it to reach thermal equilibrium before wetting simulations were conducted (see Chapter 4 for more information on the temperature behavior of the substrate during wetting simulations). The average damping was thus discretized into $\gamma = 0.000004$ eV-ps/Å^2 increments spanning $0 \leq \gamma \leq 0.000100$ eV-ps/Å^2, creating a damping region with an average damping consistent with that described above.

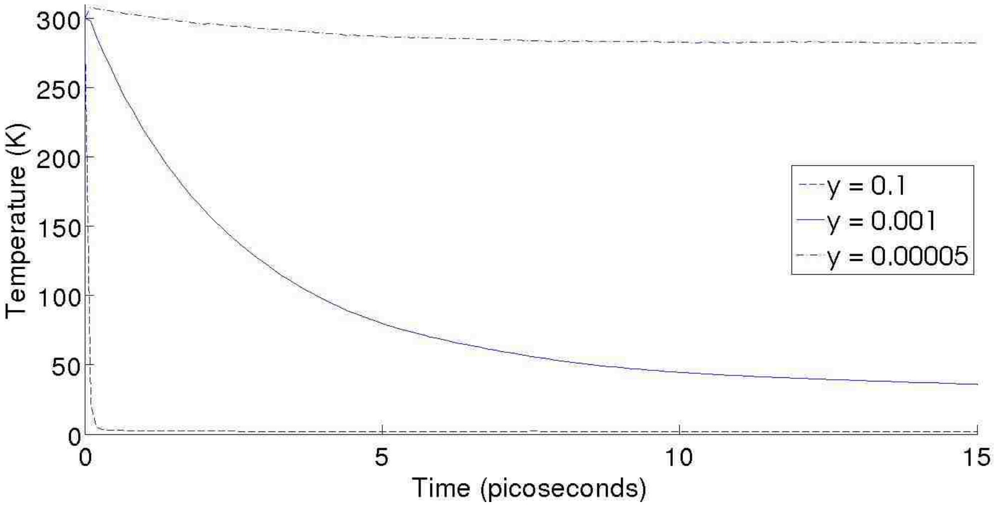

Figure 3.3 Average temperature vs. time for Al substrate NVT region, with varying damping coefficients γ, as labeled, in damping units of eV-ps/Å^2.

3.3 System validation testing

The procedure presented so far establishes an equilibrated system consisting of a cylindrical liquid Cu drop and solid rectangular Al block approximating that of an infinitely deep solid in a common simulation box. These were initially positioned so as to be outside of interaction range with one another for the potential model at time $t = 0$ ps. Given this, it was necessary to ensure, before any observations of wetting behavior were made, that the boundary conditions applied to the substrate model would behave as a system in a way consistent with what had been predicted by the individual preparations described above. To this end, trial simulations were run in which a Cu(*l*) drop at T = 1500 K, with diameter D = 40 nm and velocity v = 400 m/s, normal to the surface, was launched at the Al substrate surface; the goal of such simulations was to monitor pressure waves within the substrate to ensure that any waves generated by drop impact would be attenuated by the viscous region. The drop diameter was chosen to be nearly the maximum dimension given the model substrate dimensions and our heuristic requirement that L_x of the substrate be at least four times the diameter of the drop at t = 0. It was desired that the diameter and velocity of the drop simulated in these tests was sufficiently great to represent the maximum impact scenario for which this model had been developed; the maximum allowable velocity was determined, as will be explained further in Chapter 4, as that at which the kinetic energy of the impacting drop creates noticeable positive z velocity in the impacting fluid (ie. the onset of ejecta is observed upon impact).

With the impact conditions of the drop so decided, and based on published data for the speed of sound within Al, the travel time for a wave to propagate from the surface of the substrate, reflect off of the bottom frozen region, and reach the surface again was calculated. Because the mechanical properties of the Al model used in these simulations have been shown to compare favorably with experiments (see Chapter 2), the speed of sound within the model Al substrate was estimated as that of pure Al at T = 300 K as $c_{Al} \approx$ 6400 m/s. This was used to compute the expected time of pressure wave reflection was calculated; given the depth in z of the Al block, and with the understanding that partial attenuation in the viscous region could—in the case that that region did not completely damp all of a reflecting pressure wave—alter the travel time of such a wave, the approximate time for a pressure wave to reach the substrate surface was estimated to be ~ 7 ps. Figure 3.4 shows pressure fluctuations in the z direction of atoms at discrete z depths of the substrate. It can be seen that, though there is noticeable fluctuation in the pressure seen in the area immediately adjacent to the frozen region within the substrate, the plots of pressure in the atoms directly adjacent to the surface NVE region indicate that there is no spike in pressure seen by the atoms near the surface (ie. the atoms at the top of the NVT region)which would indicate that any waves penetrating towards the frozen region through the viscous region are allowed to travel back through to the substrate surface. The pressure in atoms centered about the negative z axis were observed for more than twice the expected period of pressure wave reflection so that any reflected components of such a wave might be observed, if present, even beyond the expected travel time through the substrate.

(a)

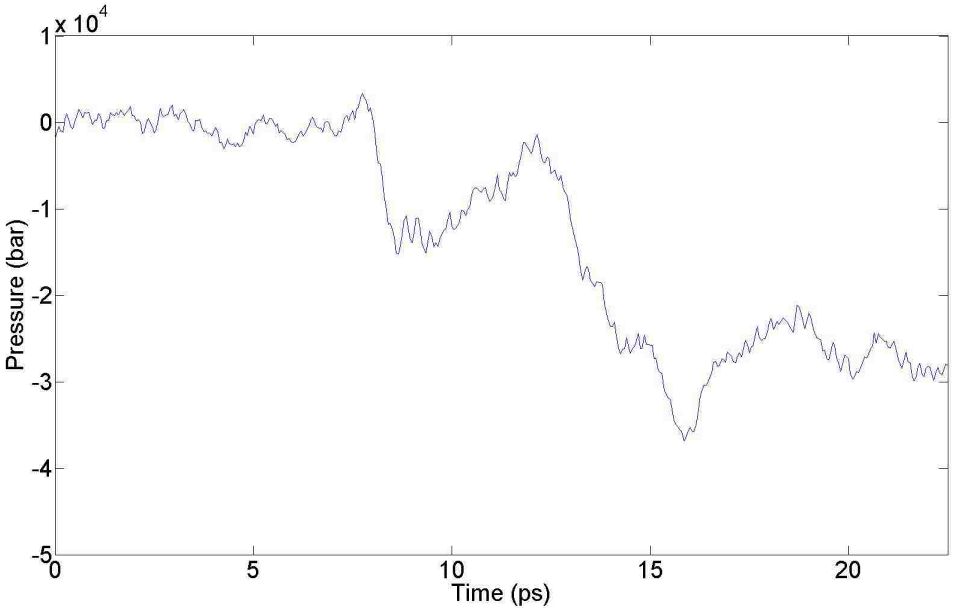

(b)

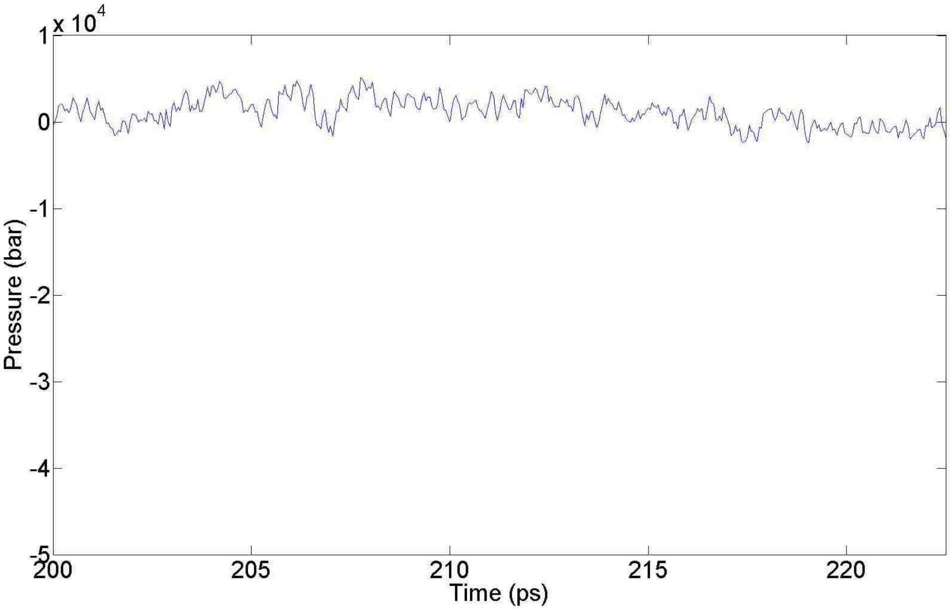
x 10^4
1
0
-1
-2
-3
-4
-5
Pressure (bar)
200
205
210
215
220
Time (ps)

(c)

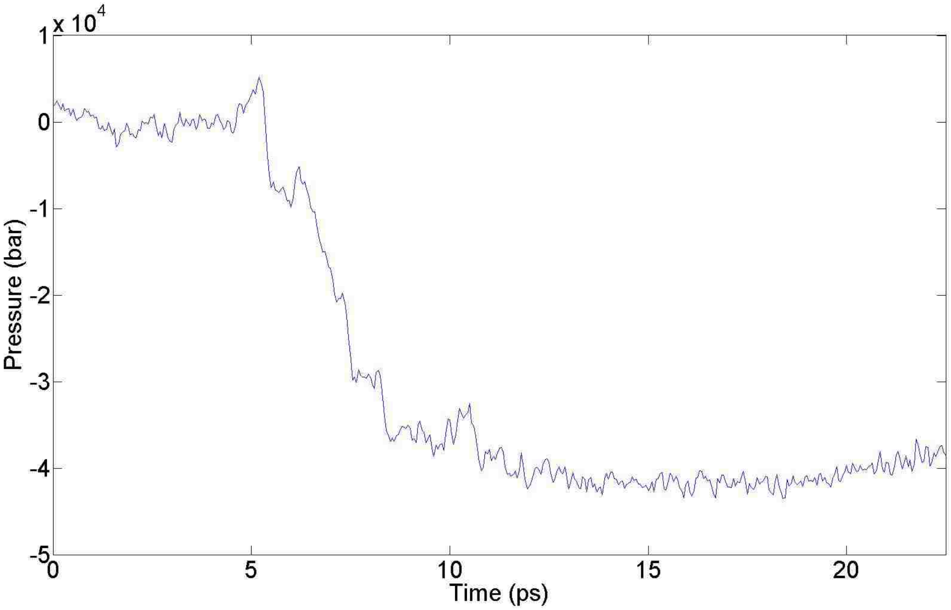
x 10^4
1
0
-1
-2
-3
-4
-5
Pressure (bar)
0
5
10
15
20
Time (ps)

(d)

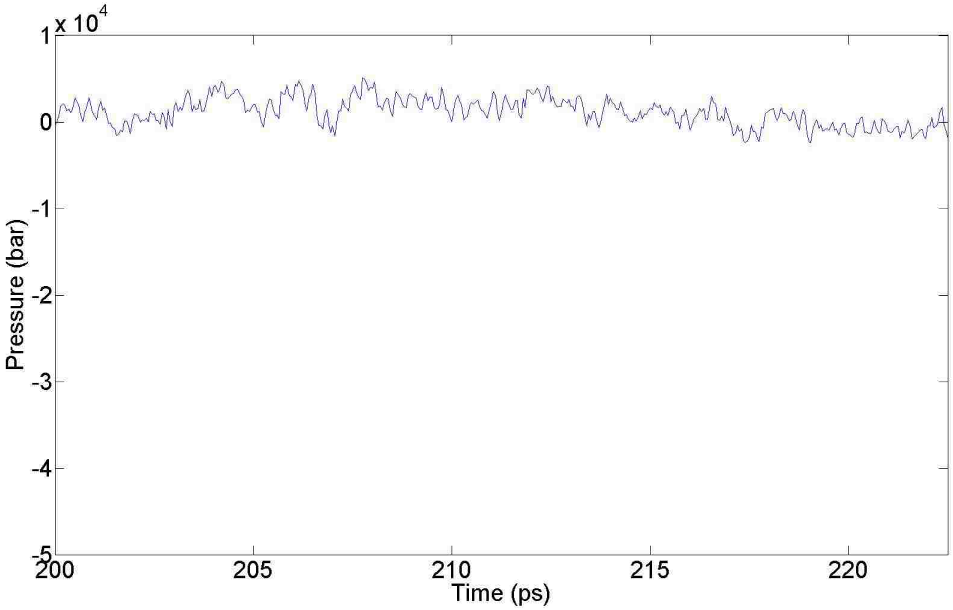

Figure 3.4 Averaged z component of stress in sections of the Al substrate; (a) and (b) show pressure in the space defined by -2.5 < x < 2.5 nm, -21 < z < -20 nm (immediately above the frozen region) for early and late times in the simulation, as shown on the horizontal plot axes. Plots (c) and (d) show pressure in the space defined by -2.5 < x < 2.5 nm, -6.5 < z <-5.5 nm (immediately below the NVE region) for similar early and late times. Note that there is no discernible pressure spike in (c) to indicate a pressure wave has reflected back from the frozen region. Note also that there is approximately zero residual stress in both test sections indicated by pressure plots at late time.

While pressure waves in the z direction of the substrate were of primary concern during this testing, it was also considered that waves traveling at the upper free surface of the substrate—the wetted surface—might also influence the wetting dynamics of the spreading drop. Though there was no viscous damping applied in the lateral, x dimension of the substrate, it was anticipated that any component of a pressure wave generated along the upper surface would be negligible. Additionally, it was expected that the advancing interface between the Cu(*l*) drop and the Al substrate—and thus the temporally decreasing distance between the contact line and periodic boundary—would generate an oscillating pressure wave of decreasing period. Nevertheless, pressure in the x direction was observed over time greater than that predicted for a wave to propagate over the distance of half of the substrate's x dimension to the periodic boundary in x and back (~ 30 ps). The results of that analysis indicate that a significant pressure wave was not reflected between the drop's contact line across the periodic boundary; indeed, no significant pressure fluctuation could be discerned in the section of Al near the substrate surface during the simulation.

Finally, to ensure that there were no pressure fluctuations within the Al substrate beyond the initial impact timespan, and to observe whether the drop impact had caused plastic deformation within the substrate material, the z component of pressure in the substrate was measured over time late in the simulation, well after the drop radius had ceased growing. Figures 3.4 (b) and (d) show the results of these observations; residual pressure, and thus stress, is shown to be negligible. These plots, in conjunction with the others shown in Figures 3.4 and 3.5, indicate that sufficient attenuation of pressure waves generated by the impact of a D = 40 nm, v = 400 m/s Cu(l) drop on the Al substrate is achieved in our model. The model tested was a simulation of drop impact with kinetic energy at least four times that of simulations undertaken in our study.

3.4 Wetting nomenclature

Consider the physical system to be modeled. An isothermal drop with non-negligible kinetic energy impacts an isothermal substrate coupled to thermal and mechanical reservoirs. The drop spreads as it wets the surface of the substrate, cools by transferring energy to the substrate, and solidifies. As a result of this action, the substrate is heated near the drop-substrate interface—possibly to melting—and eventually cools back to the original temperature $T_{SUBST.}$ due to energy absorption by the thermal reservoir.

Before detailing the results of any simulations, it is prudent to first resolve the nomenclature to be used in describing the behavior seen in those simulations. Previous sections have presented varying degrees of precision in referencing various physical formations and mechanisms associated with wetting behavior. The academic descriptions of wetting refer to constituent parts of a system based on the observation of non-reactive wetting. As a result, the liquid body which is defined as wetting a solid body is referred to as a “drop”. The solid body which the drop wets is called a “surface”. Upon contact with the surface, the drop is often said to “spread” across the surface as it wets it, and here arises a subtlety in differentiating wetting and spreading which is not particularly clear; a drop is said to wet a surface, and the behavior by which it covers a solid surface is called wetting, however a drop is also said to spread over the surface during wetting and the notion of “spreading behavior” is sometimes introduced. Wetting has been defined in Chapter 1, and is taken to be the more rigorous phenomenological term for the process of a liquid covering a solid. Spreading, on the other hand, presents itself as a more general term which describes the actual contact line advancement, or dynamic aspect, of liquid wetting. Thus wetting is the phenomena, and spreading is a more specific—though less scientific—term given to the process of contact line advancement typical of dynamic wetting behavior. In the same way that all squares can be characterized as rectangles but not every rectangle as a square, all liquid drops in contact with a surface are defined as wetting that surface, regardless of contact line velocity v_{CL}, but only those still in the process of dynamically wetting the surface (ie. $v_{CL} > 0$) can be said to be spreading over the surface.

These terms so defined, at least within the confines of this paper, there remains the resolution of industrially-derived practical terms regarding wetting related to thermal spray processes. With perhaps two exceptions, terms regarding constituent parts of wetting behavior in thermal spray processes will be referred to using the academic terminology presented above in place of any more common terms applied in industry. The impacting, deforming particle (or drop) is often referred to as a “splat” in more process-related thermal spray literature, regardless of whether the particle was solid or liquid upon impact. The particles so often generalized in thermal spray descriptions are abandoned in favor of the hydrodynamically-derived designation of drop herein. However, there will be a distinction made in describing the solid which the drop wets; whereas theoretical descriptions of wetting behavior assume an inert solid surface, reactive wetting simulations involve more than just the surface of any solid, and thus the solid bodies described henceforth will be referred to as substrates and not simply surfaces. Instead, the latter designation will only be used in describing the face of the substrate upon which the drop spreads. Figure 3.2 can be referenced to clarify this final point as well as to emphasize that a drop will be referred to as such for the duration of the simulated wetting and solidification process.

4. Simulation Results

4.1 Introduction

Features of thermal spray processes along with terminology have been presented in Chapter 2 and 3, and details of simulation parameters and methods are discussed in Chapter 3. This chapter will detail the results of a single liquid Cu(*l*) drop impacting a solid Al surface to examine the partial wetting behavior of kinetic high temperature liquids. Specifically, we examine the morphology formation of a solidified drop after impact and spreading. Particular attention is paid to mechanisms of contact line advancement in conjunction with atomic thermophysical behavior at the evolving solid-liquid interface.

MD simulations were conducted of reactive wetting of a cylindrical Cu drop onto solid Al. Input parameters were chosen to approximate those observed in thermal spray processes. Though there is no defined limit to the system size which can be modeled using the LAMMPS software package, as described in detail in the preceding chapters, care must be taken when designing a system so as to balance size with computing time required to appropriately simulate a given system over a suitably long enough time. Because the goal of carrying out these high temperature, reactive capillary simulations is an academic one—namely, to study such wetting behavior quantitatively in a way which has not been undertaken before, and to present those findings to the scientific community to further the understanding of wetting behavior—the calculations are idealized. Aforementioned variables such as surface topography or chemistry are removed from the system and the focus is placed on the solid-liquid interface formation.

Whereas the size of liquid drop and solid substrate, and the reasoning behind those dimensions, have already been established, the variable of drop velocity remained as the second independent variable along with drop diameter. While both independent, considerations were made so that the combination of drop size and velocity did not overwhelm the capabilities of the system. Specifically, three events needed to be avoided over the duration of the simulations to ensure the viability of any results obtained from them. Mixing of atoms from non-thermostatted and thermostatted substrate regions, Cu drop ejecta, formed during drop impact, crossing over imposed periodic boundaries, and spreading Cu drop material on the substrate surface crossing over periodic boundaries are all to be avoided. These criteria are important in the maintaining of a simulation which models *only* the wetting behavior of a single high temperature Cu drop with non-zero initial impact velocity onto a solid Al substrate of semi-infinite size.

Mixing of thermostatted and non-thermostatted atoms is important to avoid because the thermostat algorithm acts on instantaneous velocities to maintain the NVT region at a set temperature. We wish to model flow of the impacting drop, which is related to time averaged, translational velocity. Thus a thermostat algorithm acting on instantaneous atomic velocities can directly alter flow behavior in non-physical ways. Because the drop temperature is initially significantly greater than the temperature of the substrate, some melting will occur near the surface in the solid substrate. Liquefaction of substrate material abets mixing between the drop and substrate. The depth to which this thermally-driven mixing will propagate into the substrate is also dependent upon the mechanical damage introduced by the kinetic energy of the impinging drop. Mixing with NVT substrate material will occur if sufficient thermal and kinetic energy are imparted to the substrate to drive melting down from the impact surface to this region. This may produce an artificial influence on wetting behavior of the drop. This scenario is highly undesirable, as it sheds considerable doubt onto the validity of any results obtained from such a simulated system due to the unphysical energy dissipation which the presence of a temperature control algorithm (thermostat controller) very near to the drop material would incur. Relevant thermal spray process velocities can still be accessed without hurting the fidelity of the model, but the limited size of the drop means that the resulting Reynolds number of the flow is extremely small compared to macroscale flow regimes.

The latter two situations that must be avoided are both examples where drop material reaches the edge of the simulated domain. Though the drop flow is in the regime $Re \ll 1$, its velocity may become high enough for splashing to initiate. This highly complicated behavior will be the subject of future work; in the interest of avoiding the onset of drop splashing, an upper limit was placed on the velocities studied which corresponded with observed splashing behavior. Drop-drop interactions across periodic bounds is another concern having to do with the necessary boundary conditions imposed upon the simulated system so as keep it constrained in a way that drop wetting behavior can be taken to be physical. Sufficiently high impact velocity of the drop has been shown, in a few early simulations with this system, to cause a significant amount of substrate and drop material to be ejected from the impact site. This material can, if the simulation box boundaries are not placed sufficiently far from the impact site, cross the horizontal periodic bound to interact with other ejected material or cross the vertical bound to interact with the underside of the substrate block. Even in the absence of splash initiation, the drop may spread sufficiently to reach the periodic boundary conditions in x, thus interacting with itself and destroying the integrity of an isolated drop model. These qualitative considerations placed an upper bound on velocity studied and permitted better understanding of the resources required to model more complicated phenomena such as splashing. While the specifics of such behavior may in the future be of interest to study, for the sake of the current investigation such behavior is not necessarily unphysical, but nonetheless undesirable.

The impacts were simulated normal to the surface, along the z axis of the simulation space. Due to the pseudo-two-dimensional nature of the simulations resulting from the periodic boundary conditions in the y direction, characterizations of the system were made in the x-z plane. The x axis thus corresponds to the spreading dimension and is therefore regarded as the radial axis of the drop; the z axis in the simulation is positioned such that $z = 0$ is the initial position of the solid-liquid interface. Thus, the z axis essentially measures distance from this interface—albeit, assuming this position is undisturbed by the impact and dissolution at the reactive wetting interface.

As shown previously for the Al model employed in these simulations, the equilibrium lattice constant at $T = 300$ K was measured to be 4.0856 Å. For solid fcc Al in the (001) orientation, then, the spacing between the centers of atomic planes in the z direction is roughly 0.2 nm. This 0.2 nm atomic layer was more meaningful in delineating the various layers within the substrate, as described in Chapter 3. The measure forms the basic length scale employed in all of the simulation analyses, however. The substrate crystallographic length scale is our primary reference however; after solidification of the drop, the Cu lattice planar spacing is also a relevant length scale. This too is close to 0.2 nm. Though solid Cu has a slightly different lattice constant than solid Al, the difference is negligible and, moreover, unimportant. The discretization length scale of 0.2 nm is sufficient to bear out subsequent discussion.

Figure 4.1 shows a schematic representation of a drop at some time after impacting a reactive surface. The configuration of the drop relative to the surface and coordinate axes is consistent with what is used in the current study's simulations, though the scale is not. To illustrate what happens to the substrate near the contact line, and especially the destruction of a solid surface at the interface, mixing and deformation of the substrate is shown in the schematic. It is important to note that subsequent analyses will be aimed at characterizing the dynamics of molten material primarily above the plane representing the original substrate surface. This is done for consistency across simulations where the substrate may melt by varying amounts and also for uniformity of interpreting results between analyses. Thus a plane near the original solid surface is superimposed over the spreading drop as reference throughout all simulation analyses.

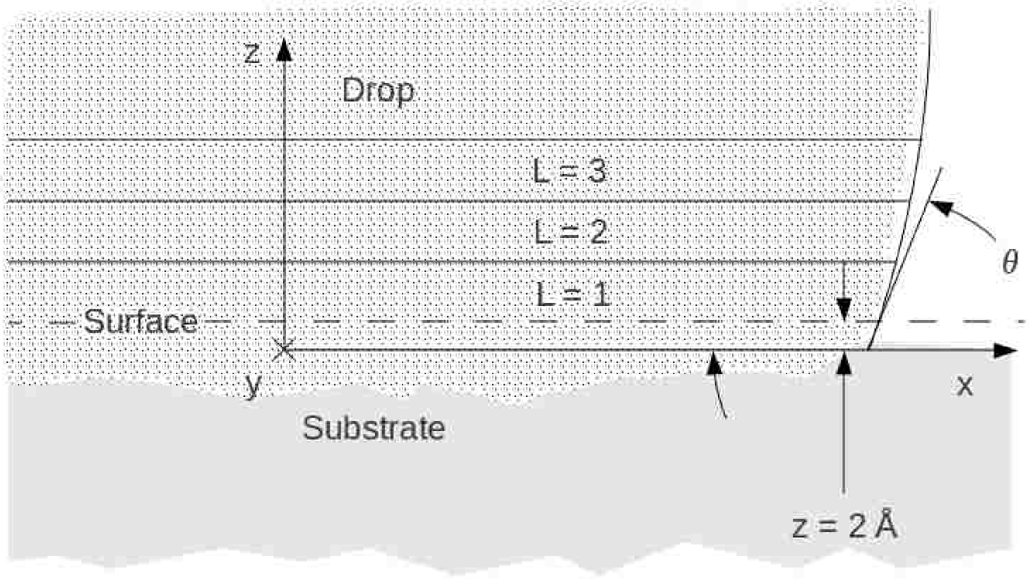

Figure 4.1 Cross-sectional schematic of cylindrical drop wetting flat surface. Note that the drawing is not to scale. Drop shape is approximated. Dissolution and surface deformation are represented. Note that the drawing is not to scale

Though it has been established that the substrate surface began the simulations with a perfect crystalline structure and an uppermost atomic plane at z = 0 nm, all measurements of the drop with respect to height above the surface are measured for z = 0.2 nm and larger. This is because drop impact can cause substrate atoms at the free surface to oscillate upward in z a somewhat larger amount than normal. Though the number of such events is small, they confound a straightforward definition that all material with $z > 0$ is part of the drop. For instance, such an anomalous free surface atomic oscillation can make it seem as if drop material exists on the substrate in places where it does not. Introducing a small (0.2 nm) spatial filter prevents such erroneous data contributions while still allowing for a straightforward definition of drop material (ie. $z > 0.2$ nm). Note that anomalous free surface atomic oscillations occur in the absence of drop impact, albeit with lower probability. For this reason, a spatial filter like what is used here is often used in MD simulations of isothermal sessile drop wetting phenomena as well.

4.2 Contact line advancement

For radius analyses, vertical “levels” of spacing equal to 0.6 nm are used to discretize measurement in the z direction (see L = 1, 2, 3, ... in Figure 4.1) and calculations are based on the average radius over each level. The 0.6 nm increments represents only 1.5% of the total starting diameter of the original droplet and roughly 2% of the final drop height after spreading, and thus is taken to be a sufficiently fine span over which to average the radius. At the same time, such height discretization allows simplified visualization of the R(t) data at heights above the surface on common axes. This was necessary because the exact contact line is difficult to distinguish when individual atomic spacing is not negligible compared to the size of the drop itself (See Figure 4.2). Measuring the radius of only Cu(*l*) drop material explicitly at the intersection with the surface without including dissolved Al(*l*) substrate material may not accurately represent the actual radius of the liquid drop.

As a prelude to quantitative results, Figure 4.2 shows a computer-rendered snapshot progression of a simulation in LAMMPS with the physical system geometry specified in Chapter 3. The velocity of the drop in Figure 4.2 is near the upper bound of what is possible with the currently implemented model. The images serve to provide examples of some of the physical features of a high temperature, impacting and reacting wetting drop.

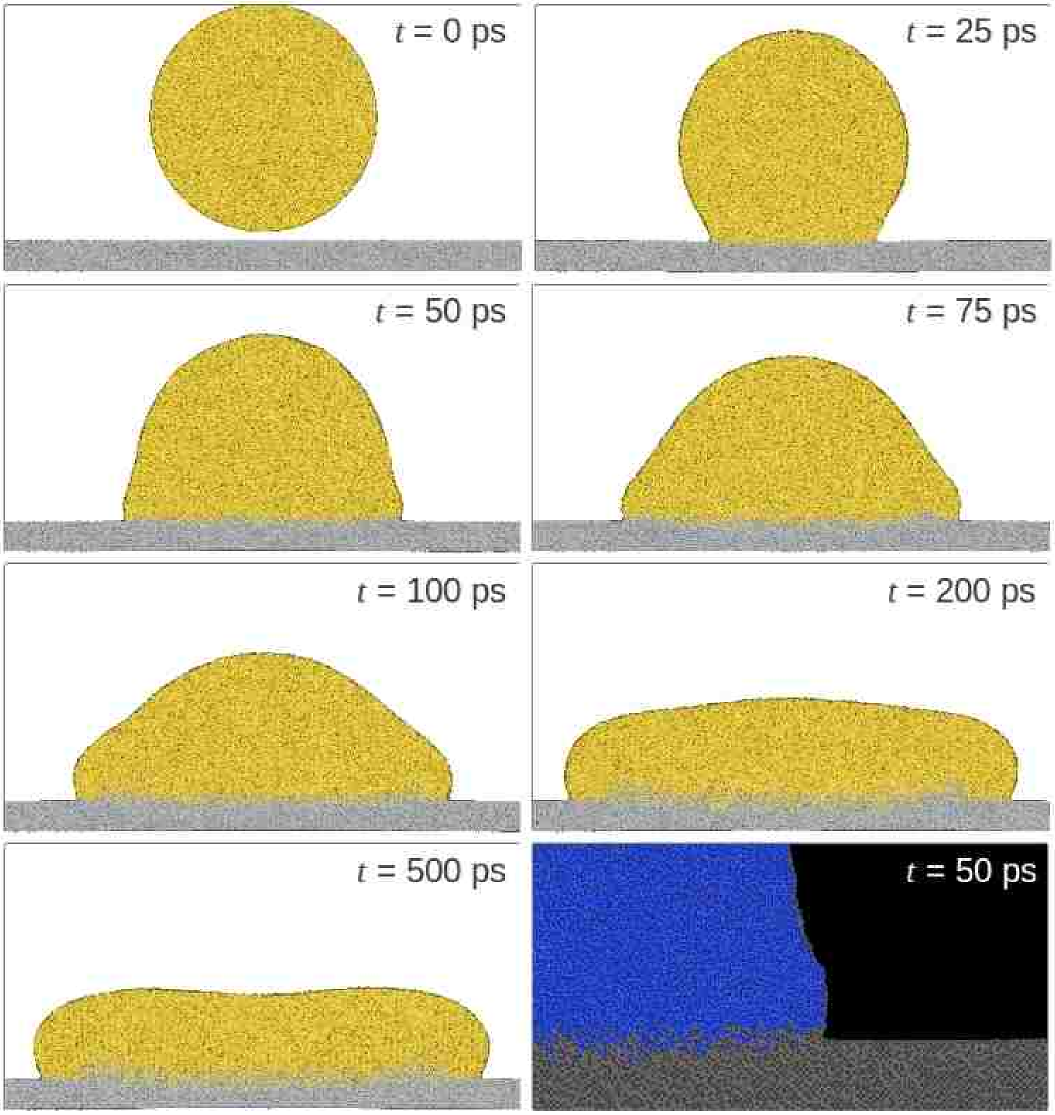

Figure 4.2 (color online) Snapshots of Cu(*l*) drop spreading on Al substrate, with initial drop velocity v = 200 m/s and normal incidence angle. The entire depth of the substrate is not depicted. Timestamps represent simulation time. Note the bottom-rightmost view is a detail of the contact line area, with colors altered.

4.2.1 Radius vs. time

Having established specific wetting characteristics to be avoided, appropriate boundary conditions, and equilibrated system dimensions and input parameters, then, it is appropriate to examine a single state point for detailed investigation into wetting behavior, and discussion regarding such behavior. To demonstrate the work being done to investigate high temperature capillary behavior via MD, the state point characterized by an initial drop velocity of v = 50 m/s and drop diameter D = 40 nm was conducted. Analyses of the results of this simulation are presented, as well as discussion regarding their implications with respect to wetting phenomena.

Figure 4.3 presents a rendered snapshot progression of atom positions for the state point to be analyzed. The flattening of the drop at the 50 m/s impact velocity is less than that of the 200 m/s case, owing to the decreased kinetic energy carried by the drop at impact. Radial growth ceases before the drop has spread significantly on the substrate due to dissipation of energy through mechanisms such as those discussed in Chapter 2. In addition, in this simulation, solidification of drop material acts to slow and eventually halt spreading. Radius curves for successive levels above the substrate surface are presented in Figure 4.4. It should be remembered that at t = 0 ps the drop is 1 nm above the surface. Splat radius plots for successive levels above the substrate thus begin at a non-zero length value corresponding to half the chord length of the drop at that height (note the curves corresponding with levels further above the surface begin at a non-zero value, reinforcing this point).

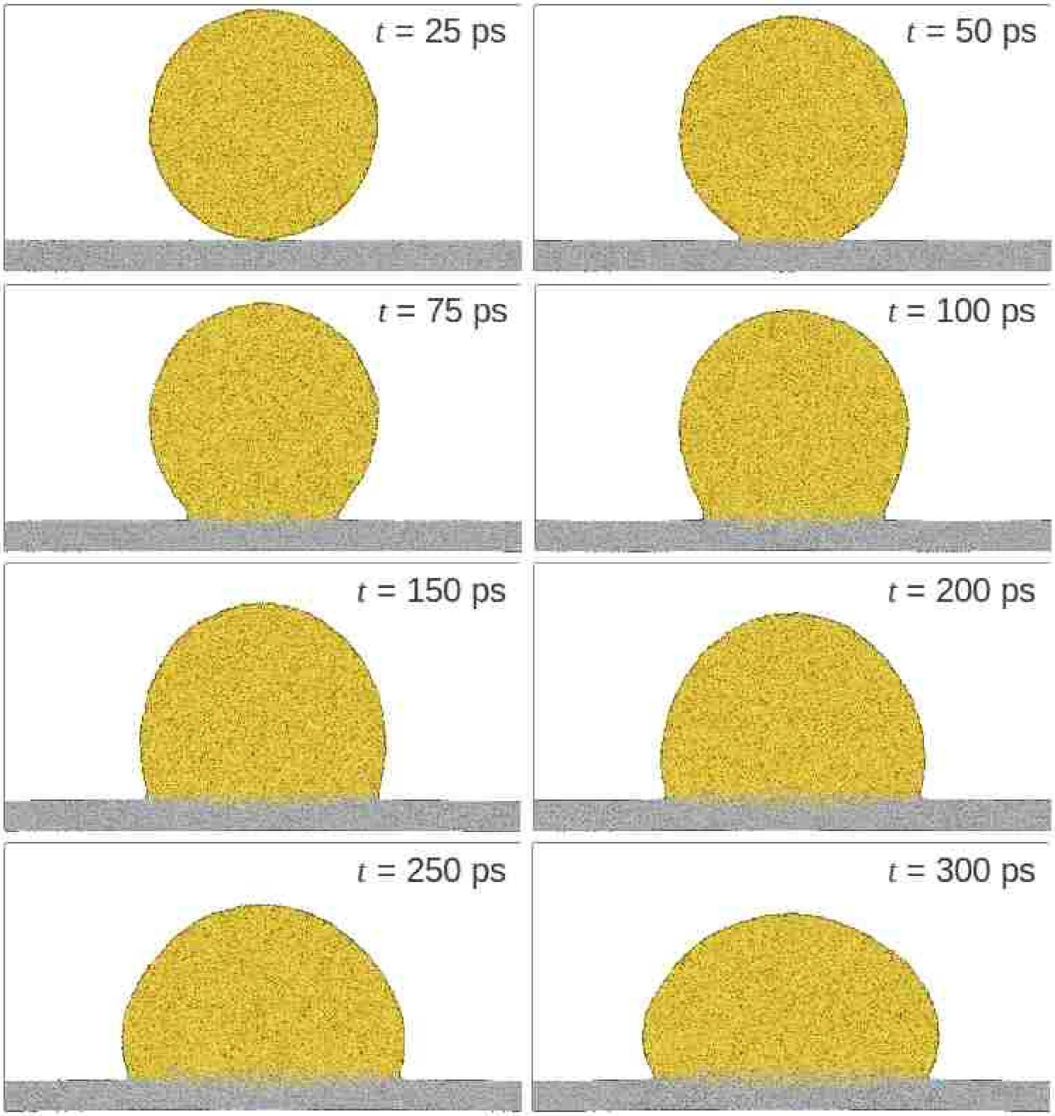

Figure 4.3 (color online) Snapshots of Cu(l) drop spreading on Al substrate. Initial drop velocity is $v = 50$ m/s. Note that the plot of radius vs. time indicates that the radial spreading of the drop has approximately ceased, and thus further frames beyond $t = 300$ ps are not shown. Flattening of the drop is less pronounced than in the $v = 200$ m/s case of Figure 4.2. Nonetheless, mixing at the solid/liquid interface can be observed.

(a)

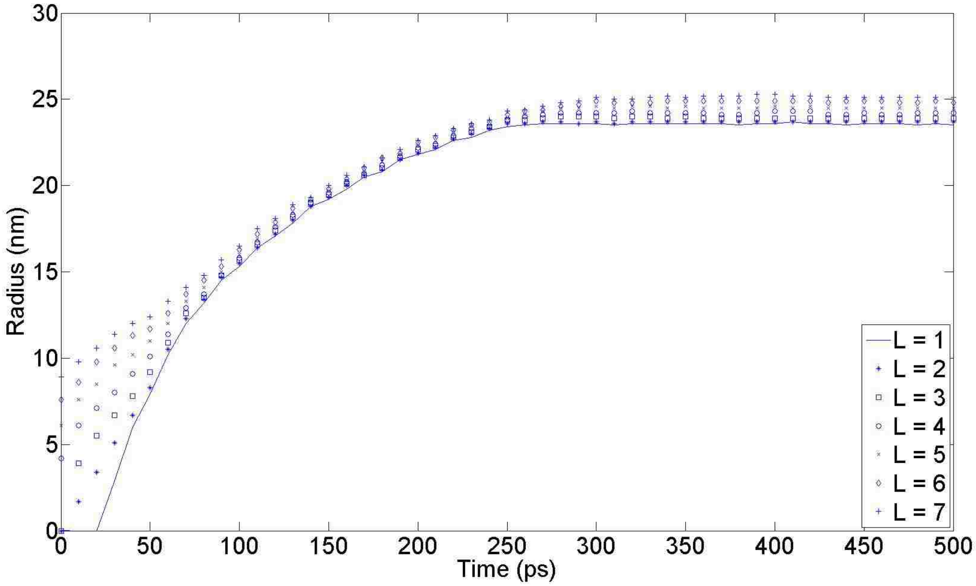

(b)

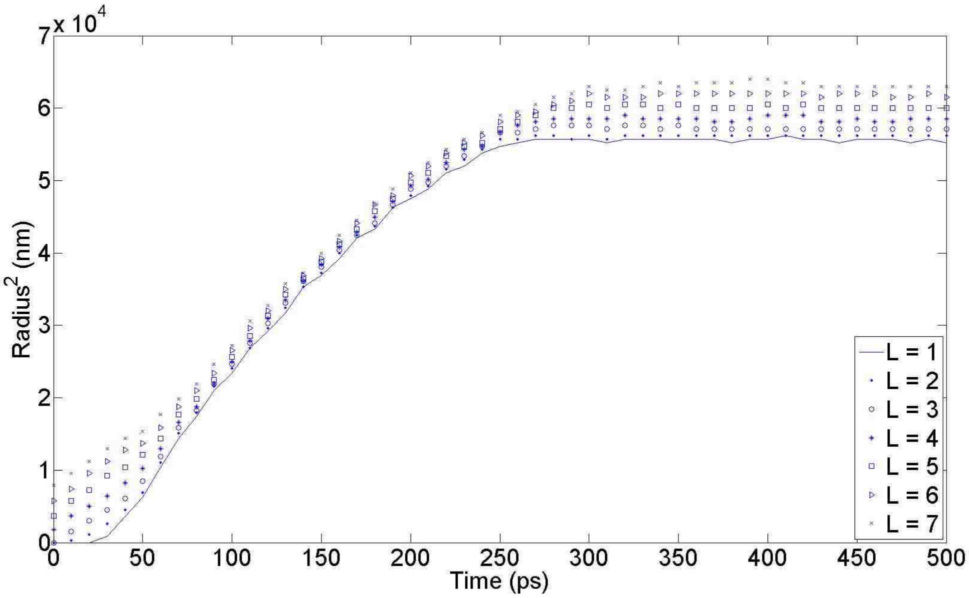

Figure 4.4 (a) Radius and (b) Radius^2 vs. time for Cu(*l*) drop wetting Al, with curves for each of the first seven levels above the surface ($0.2 \le z \le 4.4$ nm).

It can be seen from these results that the only spreading regime exhibited is an inertial one before spreading essentially halts at *t* = 250 ps. This is not surprising since Figure

4.3 shows that non-constant curvature exists in the liquid/vapor interface during most of the spreading duration (this is particularly evident near the contact line). Future work will investigate whether spreading regimes beyond inertial are exhibited for higher impact velocity drops.

4.2.2 Contact angle vs. time

Radius $R(t)$ and contact angle $\theta(t)$ are the two dimensions by which wetting kinetics are typically described. These two quantities are evaluated for the reactive wetting system in our study for comparison with macroscale descriptions of drop wetting, though parallels between macroscale nonreactive wetting and nanoscale reactive wetting have not been drawn as of yet. For the high temperature nanoscale drop examined herein, the evolution of the contact angle as a function of time, $\theta(t)$ is shown in Figure 4.5. At initial time $t = 0$ ps, there is no contact angle, owing to the fact that the drop still has yet to make contact with the surface. Upon contact with the substrate, the drop's contact angle is initially very high. However, within the first ~ 75 ps the contact angle rapidly decreases to an average steady state value of roughly $\theta = 110^\circ$. Significant changes in θ cease after $t = 100$ ps.

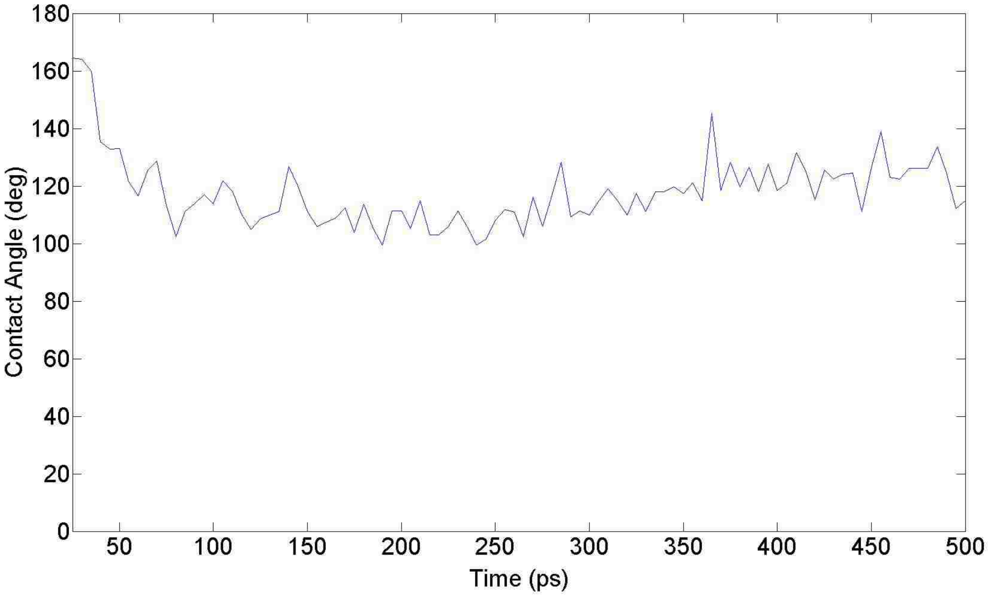

Figure 4.5 Contact angle progression for Cu(l) wetting Al(001) at T = 1500 K. Drop velocity at impact is v = 50 m/s.

Comparing contact angle and radius plots as a function of time, it becomes clear that despite the continued radial increase in splat contact area for roughly 100 ps < t < 250 ps, the contact angle remains at a nearly constant value. In other words, $\theta(t)$ is constant while $\frac{dR}{dt}$ is changing. This is in contrast to wetting theory that assumes $\theta(t)$ is a measure of how far a system is out of capillary equilibrium and, therefore, directly correlates with spreading rate $\frac{dR}{dt}$. Here, the change in radius versus time and $\theta(t)$ appear decorrelated. Note that, after spreading ceases near t = 250 ps, the contact angle increases slightly to $\theta \approx 120^\circ$. This appears to be a result of remnant drop momentum in z. Because the contact line no longer advances, drop material farther from the solid/liquid interface is forced outward in the spreading direction (see the last two frames of Figure 4.3). This gives a higher contact angle.

4.2.3 Drop wetting morphology

The process of drop wetting can thus be divided into two distinct phases based on wetting driving mechanisms. The first phase, characterized by a nearly linear growth of the radius of the spreading drop, can be viewed as the initial inertially-driven regime. The second phase is dominated by solidification. For the current state point under examination (v = 50 m/s, D = 400 A), the impact velocity can be said to be relatively modest. Compared to the speed of sound in air at sea level, for instance, 50 m/s would represent a Mach number of M = 0.15—hardly enough to be considered in a compressible flow regime. It must be noted that the simulation is of a drop traveling in a true vacuum without the presence of any vapor phase surrounding the drop and substrate, but the comparison of drop velocity to the speed of sound is one that compares readily with more traditional fluid dynamics studies in which Mach number is very commonly referenced. A more physically similar velocity comparison can be made to actual thermal spray processes such as vacuum plasma spraying (VPS) in which particle velocities in excess of 1500 m/s are typical. By this metric, the simulated drop's velocity is unequivocally small. This is not to say that the wetting behavior exhibited by the drop is somehow unnatural; instead, the study is one carried out on a much less extreme model of a physical system, in which the robustness of the physical model and volume of data available through MD simulations allows the subtleties—and thus the driving physical mechanisms—of such a system to be analyzed in great detail.

Due to the relatively low inertia which the drop is carrying upon impact, along with the effect of solidification, spreading ceases quickly after impact. In fact, only an inertial regime of spreading is evident. Capillarity appears to have little to do with mechanisms driving contact line advancement in this case. This is especially important when comparing the behavior of this drop to macroscale hydrodynamic wetting theory which, as mentioned in Chapter 1, typically specifies an equilibrium contact angle for a liquid on a certain surface derived from experimental data. Note that an equilibrium contact angle for this system is very difficult to define because Cu melts at a higher temperature than Al. Therefore, any system of Cu(*l*) in contact with solid Al is necessarily a non-equilibrium one.

At a certain time, the liquid Cu drop has concluded spreading and remains partially wetting the Al surface at a contact angle roughly equivalent to the steady state advancing contact angle. From these observations, it can be concluded that the example presented is a case of inertial wetting that ceases when solidification occurs at the solid/liquid interface. Apparently, the very low Weber number drop is unable to significantly deform the liquid/vapor interface and drive flattening of the drop. From images in Figure 4.2 it can be seen that greater flattening is possible in our simulation setup. Future work will attempt to better elucidate the dependence of flattening on Weber number for nanometer scale dimension.

Because there is a temperature difference between the drop (T = 1500 K) and the substrate (T = 300 K) corresponding to roughly twice the melting point of the substrate material, heat transfer from the drop to the substrate is observed to cause localized melting in the substrate at the drop-substrate interface. This melting at the interface is also being combated by the thermal capacitance of the substrate, whose thermal reservoir characteristics are approximated by the inclusion of thermostat control at greater depths in the substrate as detailed earlier. The finite thermal energy of the drop only temporarily, locally melts the substrate. This phase change in itself constitutes a form of energy dissipation, and the net effect on drop dynamics can quantitatively be viewed in the following manner: high energy Cu(*l*) wets the Al surface, conducting heat and melting Al, which in turn dissipates Cu energy as the drop continues to wet the surface and the combination of Al thermal mass and Cu energy dissipation allows for solidification of Cu and Al which eventually propagates throughout the entire mixed interface region and through the entirety of the drop. The magnitudes of these dissipation contributions is as-yet unknown, and the temperature gradient as a function of time is the matter of future work to understand the impact that thermal energy transfer has on wetting mechanisms. Nonetheless, it can be seen for the relatively low velocity case presented that phase change mechanisms play a prominent dissipation role.

4.2.4 Thermal wetting component

Though θ(t) and R(t) are two universal measures of wetting behavior in general, for the highly reactive Cu and Al system simulations a large amount of dissolution is observed as a result of aforementioned thermal contributions. This is more pronounced for higher velocity drop impact; qualitatively, this can be derived from comparison of Figures 4.2 and 4.3. Note this is for drops with the same temperature upon impact so increased mixing is a result of increased kinetic energy, rather than thermal energy. These thermal contributions are understood to influence wetting kinetics, though to an unknown extent. To begin to characterize thermally influenced wetting behavior, an approximation of the amount of mixing which occurred between the liquefied Cu and Al was made. While it is qualitatively informative to examine dissolution based on pictures such as Figure 4.2, it is prudent to take advantage of the atomic information readily available from the MD simulation. Specifically, it is straightforward to characterize the distribution and number of Al atoms above the surface (recall, to define the separation between drop and substrate, a 0.2 nm spatial filter above the z = 0 original solid surface was employed). This measure was employed as a first step in quantifying dissolution. This method is understood to underestimate the total number of Al atoms which become liquefied and mixed with the wetting Cu atoms because it does not account for these events in the substrate. Nonetheless, such a characterization is useful in revealing the relationship of dissolution with respect to time. The results of this analysis are shown in Figure 4.7.

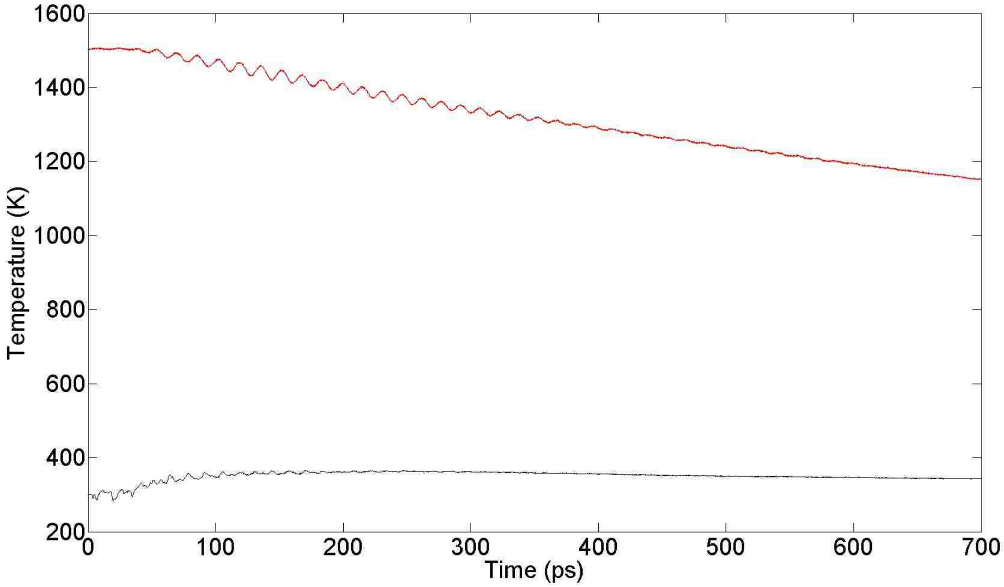

Figure 4.6 Temperature vs. time plot for Cu drop (upper curve) and Al substrate in the surface region (lower curve). Note that both curves represented the spatially-averaged temperature for the entire regions associated with them.

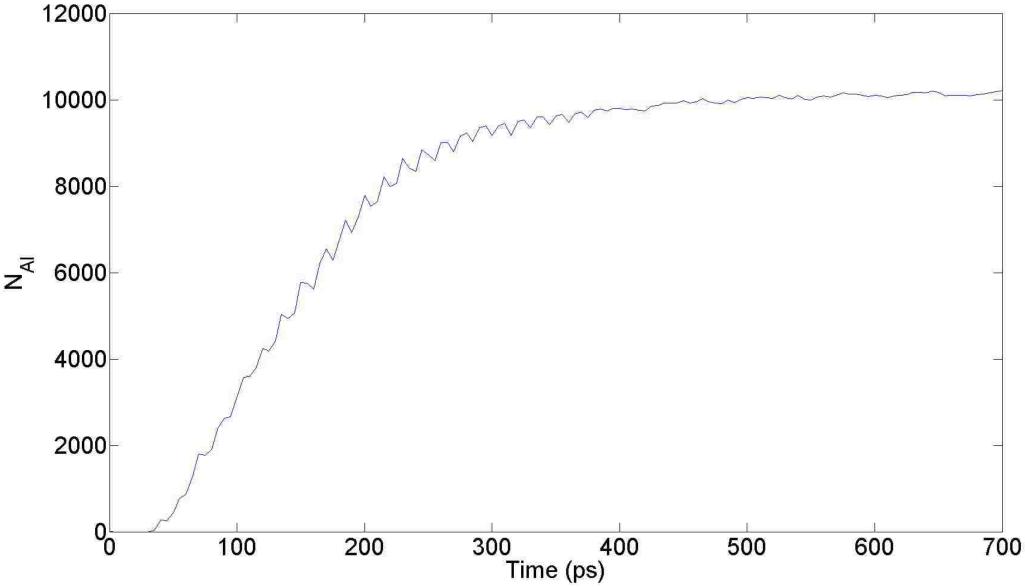

Figure 4.7 Total number of Al atoms (N_{Al}) positioned above z = 0.2 nm, as a function of time. This is given as an indication of the dissolution of Al into the Cu, inferred to be a function of the mixing between the two.

From the curve in Figure 4.7, two observations regarding our system's reactive wetting can be made: the growth in the average number of Al atoms above the substrate surface oscillates about a steadily increasing value; also, N_{Al} vs. t appears to take on a shape similar to the radius $R(t)$. The former of these two observations will be examined separately, as it pertains to questions of model integrity as well as reactive wetting. For the latter observation, note that the amount of Al atoms drawn above z = 0.2 nm continues to increase, albeit slowly, after $R(t)$ halts its increase. Near the end of the time period shown in Figure 4.7, it is apparent that Al dissolution has ceased. Dissolution kinetics resembling spreading kinetics is not surprising because increasing radius means greater interfacial area over which dissolution may occur. Indeed, it can be surmised that dividing results in Figure 4.7 by $R(t)$ data would reveal a relatively constant dissolution rate (interfacial area scales with radius because L_y in the simulation is constant). This is further evidence that phase change mechanisms couple closely with spreading kinetics and relevant dissipation.

Owing to the high heat capacity of Cu compared to Al and the temperature differential at drop impact of approximately 1200 K, it is reasonable that melting and dissolution of the Al begins very quickly after contact between Cu and Al at the wetted interface. Expansion of the Cu-Al interface as well as forced bulk fluid motion within the Cu drop drives the increase in dissolution between the two metals. Dissipation of kinetic and thermal energy throughout the first 200 ps of drop impact and splat formation, meanwhile, leads to the decrease in the rate of Al dissolution. Similar to $R(t)$, the rate of dissolution appears to become significantly decreased at roughly $t = 250$ ps. This is taken to be an indication of the onset of drop solidification. At this point, the interfacial area is no longer changing. Dissolution, while much slower, does not appear to halt until $t \approx 500 - 600$ ps.

It can be observed from the radius, dissolution, and temperature plots that a periodic oscillations are present in the data; the period of these oscillations is ~ 20 ps. The prevention of the propagation of pressure waves within the substrate was addressed in Chapter 3. Briefly, the relevant periods of any such traveling waves are ~ 7 ps (in z) and ~ 30 ps (in x). Also, because the distance between the contact line and the periodic boundary in x is decreasing, this period is expected to be non-constant. Nonetheless, these considerations seem moot in light of direct pressure data evaluated as a function of time (Figures 3.4 and 3.5), where it was shown that no evidence of traveling pressure waves exists. Thus it is suspected that the oscillations within the system are a result of energy dissipation mechanisms involving, but not necessarily limited to, temperature oscillations of the liquid and phase changes at the solid/liquid interface. At the atomic scale, as mentioned earlier, kinetic energy of the atoms directly influences the bulk velocity and temperature of an atomic ensemble, and thus the distinction between temperature of the drop as a whole, and the bulk motion of atoms within the drop, is less clear at the scales seen in atomistic simulations compared with macroscale experiments. Even if temperature data are disregarded, oscillations in N_{Al} as a function of time must still be explained. This is a very explicit calculation that leaves little to interpretation. As N_{Al} steadily increases, there is a second order behavior driving Al atoms to move back and forth across the defined plane between drop and substrate. Because there is significant interaction between drop and substrate in the form of liquefaction and solidification and the wetting dynamics of that drop, it is unclear exactly what mechanism is inducing such a vibration in the recorded data in the first 400 ps of wetting.

A possible explanation of oscillations is that solidification near the solid/liquid interface drives local material contraction as well as energy release. Again locally, heat released is absorbed by solid phase material that is close to the phase transition temperature. Such material melts, causing local expansion. Clearly, future work is needed to investigate the possibility of such phenomena and, if present, to quantify its contribution to reactive wetting dynamics.

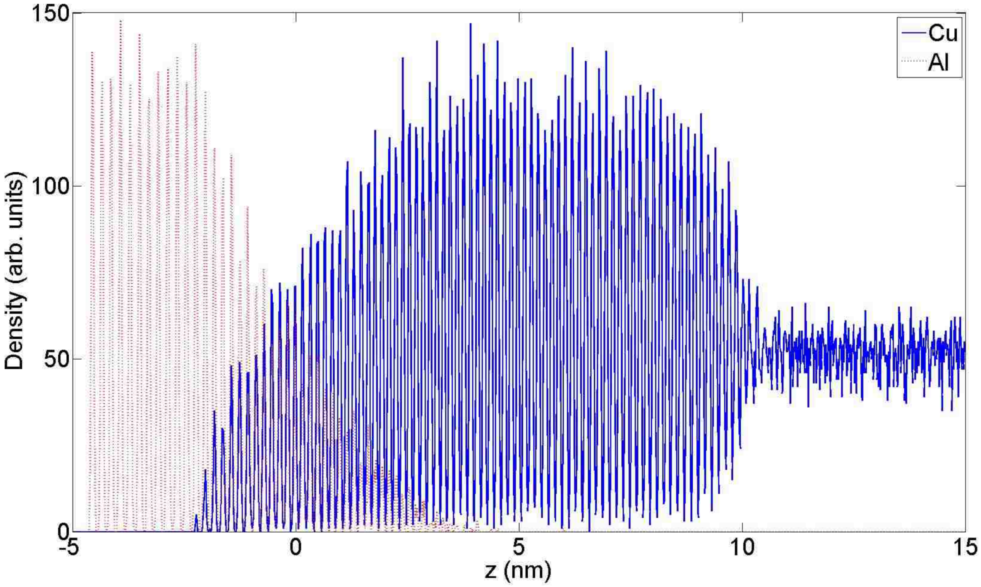

Figure 4.8 Number of Cu and Al atoms as a function of z, in the space along the centerline of the system defined by -2.5 < x < 2.5 nm and at full depth in y, for the time *t* = 700 ps. The vertical peaks are indicative of atomic planes which have formed as a result of the re-solidification of Al substrate material and the onset of Cu solidification. The decay of distinct peaks within the Cu near z = 10 nm is an indication of the solidification front within the Cu. Note that the full extent in z of the Al substrate and Cu drop material is not shown, so that atomic distributions near the Cu-Al interface can be seen more clearly.

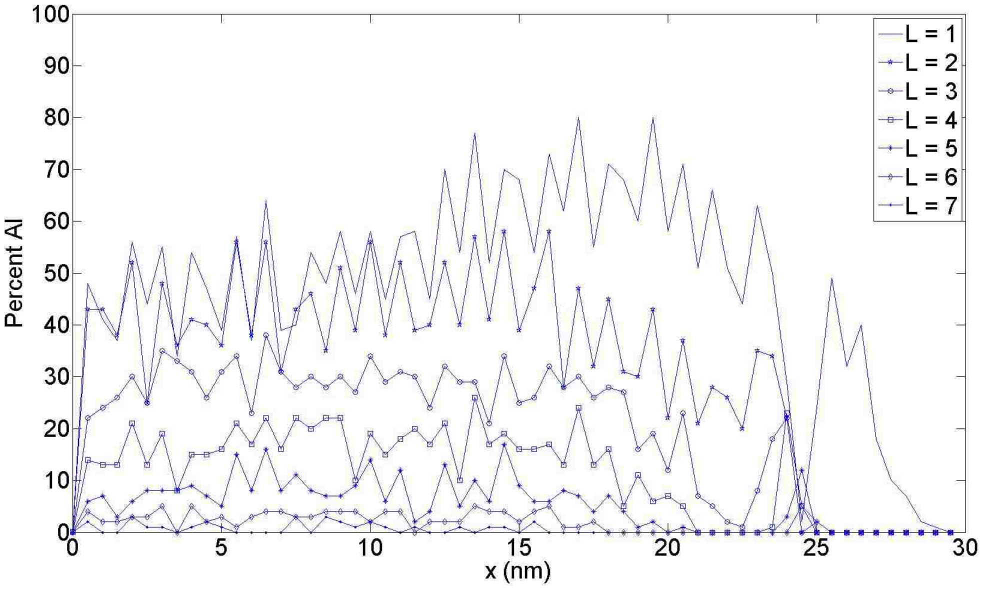

Figure 4.9 Concentration of Al with respect to distance from the centerline of the drop, calculated as a percentage of Al atoms vs. the total number of atoms contained at successive levels above the surface (z = 0.2 nm) at time *t* = 700 ps into the simulation.

To better elucidate mixing and solidification effects, density and concentration plots of Cu and Al atoms within the drop and substrate can be measured directly from MD simulations. The density distribution presented in Figure 4.8 shows the solidification and mixing of Cu and Al around the original substrate surface at z = 0 nm. It also clearly shows mixing between the two materials, their respective concentrations for the spatial region over which the density plot was generated, and the progression of solidification within the Cu at the time which atomic position data was collected for the plot. The approximate width of the intermixed region is 5 nm; note this is approximately 10 – 15% of the original drop diameter and also of the final drop height.

Figure 4.9 presents the atomic concentration of Al in Cu for successive levels above the substrate—starting at z = 0.2 nm, as explained previously. From these, the distribution of the Al can be observed within the drop as a function of z and x. In general, for each layer except level 1, Al concentration is relatively steady versus x until it drops to zero above x = 25 nm. Furthermore, levels above L = 1 show a decrease in Al concentration between 20 < x < 25 nm and then a peak increase in Al concentration near x = 25 nm, before going absolutely to zero. The concentration of Al atoms for the level L = 1, immediately above the original substrate surface plane, is of particular interest. For L = 1, the peak in Al concentration at large x occurs for x > 25 nm (ie. beyond the extent of Al in layer L = 2 and higher). These data are indicative of a plowing mechanism by which solid substrate material at early contact is melted and forced to flow to the outer edge of the advancing contact line. Indeed, preliminary evidence from higher velocity impact simulations shows this substrate plowing mechanism may relate to the onset of fragmentation (or splashing) in such systems.

The depth of information available as a direct result of this single MD simulation, for the drop of diameter D = 40 nm and velocity v = 50 m/s, motivates an ongoing study of highly reactive wetting kinetics during drop impact.

5. Conclusions and Future Work

Chapter 1 introduced the scientific phenomena of wetting and models characterizing wetting behavior for various systems. Problems surrounding descriptions of certain wetting mechanism—specifically those driving the kinetics of high temperature, highly reactive wetting systems seen in such engineering applications as thermal spray processes were also explained. A description was given of thermal spray coatings. Chapter 2 presented the principles of MD simulation models with an emphasis on those employed in the research presented herein. Chapter 3 explained the development of a robust model metallic system for high temperature capillarity simulations approximating those of certain thermal spray processes, for study of mechanisms driving nanoscale highly reactive wetting kinetics. Finally, Chapter 4 presented results from a single state point simulation.

The significance of the results of analyses presented in Chapters 3 and 4 is not that a single drop was simulated at single velocity, but in the fact that the model system behaves as intended, and the model as well as the analysis codes prepared based on it can now be used to generate data on many other state points. This data can be used to probe the mechanisms driving high temperature, highly reactive wetting behavior at the nanoscale. It is intended that insights into nanoscale wetting mechanisms will yield useful insights into highly reactive wetting behavior at the micro and macroscale. To accomplish this, work is ongoing to simulate various state points in a systematic manner, so that velocity and drop diameter (ie. Reynolds and Weber number) driven trends in system behavior can be observed in a controlled manner.

In particular, a number of features already observed in the state point analyzed in Chapter 4 exhibit interesting behavior which future work will be directed towards elucidating. Thermal oscillations in the average drop temperature, which is seen over a similar timespan—with similar period to—substrate dissolution, raises the possibility that there exists a regime of substrate-drop reaction in a harmonic melt-solidify manner that may have significant impact on wetting kinetics. Further work is required to develop and confirm such a theory, and work is ongoing to analyze temperature distributions as a function of time within the drop, interface, and substrate regions to provide a more detailed depiction of the thermal behavior of the system.

The length and velocity scale built into our MD model is near orders of magnitude seen in actual thermal spray processes, particularly those being developed in industry to produce a new class of high performance, nanostructured coatings utilizing nanoscale drops in controlled spray environments. This trend in thermal spray science and engineering means that the nanoscale drops simulated in the model presented here may indeed directly compare with those produced in actual thermal spray processes. Nonetheless, it is important to acknowledge that most thermal spray processes use larger particles. Atomic results must be used to improve continuum scale understanding of reactive wetting behavior seen in thermal spray deposition.

Finally, it is ultimately desired that our analyses of wetting at the nanoscale will allow for the interpolation of the scaling of wetting mechanisms between the macro and the nanoscale, so that more universal relationships governing reactive wetting behavior can be developed without the reliance on empirical descriptions and industrial experience for the prediction of high temperature, highly reactive wetting kinetics. To this end, the work detailed herein continues.

References

[1] P. G. De Gennes, Rev. Mod. Phys. **57**, 827 (1985).

[2] D. Bonn, Re. Mod. Phys. **81**, 739 (2007).

[3] T. Young, Philosophical Transactions of the Royal Society of London **95**, 65 (1805).

[4] D. R. Heine, G. S. Grest, and E. B. Webb III, Phys. Rev. E **70**, 1 (2004).

[5] J. B. Marion, *Classical Dynamics of Particles and Systems* (Academic Press Inc., New York, 1970).

[6] K. Landry and N. Eustathopoulos, Acta Mater. **44**, 3923 (1996).

[7] A. Mortensen, B. Drevet, and N. Eustathopoulos, Scripta Mater. **36**, 645 (1997).

[8] J. A. Warren, W. J. Boettinger, and A. R. Roosen, Acta Mater. **46**, 3247 (1998).

[9] R. Voytovych, V. Bougiouri, N. R. Calderon, J. Narciso, and N. Eustathopoulos, Acta Mater. **56**, 2237 (2008).

[10] L. Yin, B. T. Murray, S. Su, Y. Sun, Y. Efraim, H. Taitelbaum, and T. J. Singler, J. Phys.: Condens. Matter **21**, 464130 (2009).

[11] E. Saiz, M. Benhassine, J. De Coninck, and A. P. Tomsia, Scripta Mater. **62**, 934 (2010).

[12] Y. Sun and E. B. Webb III, J. Phys.: Condens. Matter **21**, 464135 (2009).

[13] L. Pawlowski, *The Science and Engineering of Thermal Spray Coatings* (John Wiley & Sons Ltd., West Sussex, 2008).

[14] P. Fauchais, M. Fukumoto, and A. Vardelle, J. Therm. Spray Technol. **13**, 337 (2004).

[15] S. Chandra and P. Fauchais, J. Therm. Spray Technol. **18**, 148 (2009).

[16] P. Fauchais, G. Montavon, R. S. Lima, and B. R. Marple, J. Phys. D: Appl. Phys. **44**, 093001 (2011).

[17] P. fauchais and A. Vardelle, J. Phys. D: Appl. Phys. **44**, 194011, (2011).

[18] K. Alamara, S. Saber-Samandari, and C. C. Berndt, Surf. Coat. Technol. **205**, 5028 (2011).

[19] K. Sabiruddin, P. P. Bandyopadhyay, G. Bolelli, and L. Lusvarghi, J. Mater. Proc. Technol. **211**, 450 (2011).

[20] K. Yang, Y. Ebisuno, K. Tanaka, M. Fukumoto, T. Yasui, and M. Yamada, Surf. Coat. Technol. **205**, 3816 (2011).

[21] E. Lang, *Coatings for High Temperature Applications* (Applied Science Publishers Ltd., Essex, 1983).

[22] C.-J. Li, H.-L. Liao, P. Gougeon, G. Montavon, and C. Coddet, Surf. Coat. Technol. **191**, 375 (2005).

[23] M. P. Allen and D. J. Tildesley, *Computer Simulations of Liquids* (Clarendon Press, Oxford, 1987).

[24] G. Sutmann, NIC Series **10**, 211 (2002).

[25] M. P. Allen, NIC Series **23**, 1 (2004).

[26] LAMMPS website: lammps.sandia.gov.

[27] M. S. Daw and M. I. Baskes, Phys. Rev. Lett. **50**, 1285 (1983).

[28] M. S. Daw and M. I. Baskes, Phys. Rev. B **29**, 6443 (1984).

[29] J. Cai and Y. Y. Ye, Phys. Rev. B **54**, 8398 (1996).

[30] E. Bertrand, T. D. Blake, and J. De Coninck, J. Phys.:Condens. Matter **21**, 464124 (2009).

[31] W. D. Callister Jr., *Fundamentals of Materials Science and Engineering* (John Wiley & Sons Inc., New York, 2001).

[32] G. McHale, M. I. Newton, and N. J. Shirtcliffe, J. Phys.: Condens. Matter **21**, 464122 (2009).

[33] L. Courbin, J. C. Bird, M. Reyssat, and H. A. Stone, J. Phys.: Condens. Matter **21**, 464127 (2009).

[34] J. Shen, J. A. Liburdy, D. V. Pence, and V. Narayanan, J. Phys.: Condens. Matter **21**, 464133 (2009).

[35] M. Marengo, C. Antonini, I. V. Roisman, C. Tropea, Curr. Op. Colloid Interface Sci. **16**, 292 (2011).

Vita

John Plumeri was born in New Jersey in 1987. He graduated from West Windsor-Plainsboro High School in 2005. He attended Lafayette College in Easton, PA, graduating cum laude in 2009 with a Bachelor of Science in Mechanical Engineering. He was awarded Best Senior Design Project in 2009 by the mechanical engineering faculty for his work designing an intake manifold for Lafayette Racing's FSAE car engine. He is currently enrolled in the Mechanical Engineering and Mechanics department at Lehigh University in Bethlehem, PA. This thesis represents the author's studies, conducted in completing his Master of Science degree.